

An in-silico approach to meniscus tissue regeneration: Modeling, numerical simulation, and experimental analysis

Elise Grosjean, Alex Keilmann, Henry Jäger, Shimi Mohanan, Claudia Redenbach, Bernd Simeon, and Christina Surulescu*

RPTU Kaiserslautern-Landau, Department of Mathematics,
Postfach 3049, 67653 Kaiserslautern, Germany

Luisa de Roy, Graciosa Teixeira, and Andreas Martin Seitz

Institute of Orthopaedic Research and Biomechanics,
Centre of Musculoskeletal Research Ulm,
University Ulm, Helmholtzstraße 14, 89081 Ulm, Germany

Martin Dauner, Carsten Linti, and Günter Schmidt

Deutsche Institute für Textil- und Faserforschung (DITF)
Koerschtalstr. 26, 73770 Denkendorf

March 12, 2024

Abstract

We develop a model the dynamics of human mesenchymal stem cells (hMSCs) and chondrocytes evolving in a nonwoven polyethylene terephthalate (PET) scaffold impregnated with hyaluron and supplied with a differentiation medium. The scaffold and the cells are assumed to be contained in a bioreactor with fluid perfusion. The differentiation of hMSCs into chondrocytes favors the production of extracellular matrix (ECM) and is influenced by fluid stress. The model takes deformations of ECM and PET scaffold into account. The scaffold structure is explicitly included by statistical assessment of the fibre distribution from CT images. The effective macroscopic equations are obtained by appropriate upscaling from dynamics on lower (microscopic and mesoscopic) scales and feature in the motility terms an explicit cell diffusion tensor encoding the assessed anisotropic scaffold structure. Numerical simulations show its influence on the overall cell and tissue dynamics.

1 Introduction

During the last decades, mathematical modeling and simulation have become valuable tools for investigating complex biomedical systems. They contribute significantly to understanding different aspects of a biological process, often allowing to extend the study to related, mutually conditioned processes. In this spirit, the present paper is concerned with modeling, simulation and experimental validation for a prominent biomedical problem, the meniscus regeneration and involved cell and tissue-level phenomena. Clinical studies indicate that partial and total meniscectomies lead to prevalence of premature osteoarthritis in knee joints. Therefore, substantial efforts are being made towards finding adequate regenerative tissue for meniscus replacement. Although there are some approaches and even commercially available products, to date the optimal substitute has not been developed. Most regenerative approaches are clinically motivated and focus rather on the practical application than on the micro- and macroscopic cellular mechanisms and the interactions with the scaffold material. The latter viewpoint is promising in the sense that it aims to understand the basic control mechanisms in cell-scaffold interactions under different environmental parameters, thus providing a selective prognosis of the most conducive combinations of

*surulescu@mathematik.uni-kl.de

these parameters.

With respect to the in-silico modeling and simulation, a major challenge lies in the well-posed and numerically efficient coupling of the processes at the cell level with the macroscopic behavior and the mechanical properties of the tissue. The active processes at the cell level, such as cell differentiation and matrix synthesis, have a strong impact on the resulting tissue structure, while macroscopic effects in turn are important stimuli for the processes at the microscopic level. Moreover, the time scales of the different processes differ vastly.

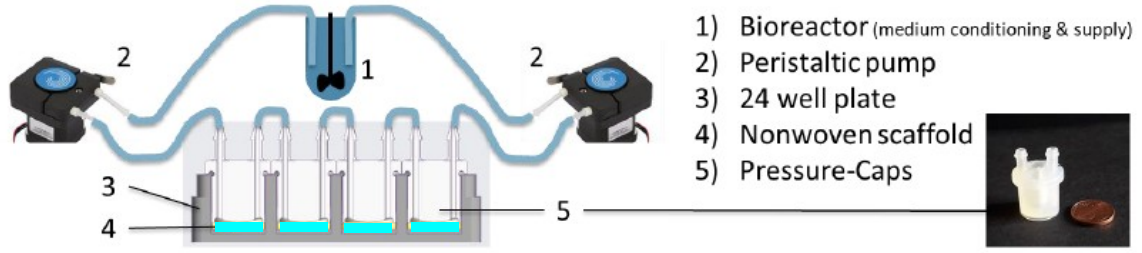
A key feature of our work is the use of accompanying experiments that are based on a nonwoven scaffold in a perfusion chamber, allowing in-vitro investigations for the development of chondrocytes and adipose tissue derived stem cells. In this framework, crucial stimuli to achieve relevant proliferation, migration and differentiation can be identified by state-of-the-art measurements. While meaningful clinical data is very difficult to obtain from the interior meniscus tissue, this off-the-wall approach provides comprehensive underpinnings for the mathematical modeling and numerical simulation.

We give next a short overview on related work and refer to [73] for a recent review of mathematical modeling in tissue regeneration in a larger sense. In spite of the increasing interest attached to meniscus tissue engineering, there are relatively few mathematical models for the dynamics of involved processes. Essential aspects concern degradation of engineered fibers, migration/differentiation of stem cells into/within the scaffold, and production of tissue by chondrocytes. Thereby, stem cell (de)differentiation seems to play a major role. It can be triggered by mechanical stress [1, 59], tissue stiffness [50], topography of the scaffold [31], or by chemical cues present in the extracellular space [29, 47, 48].

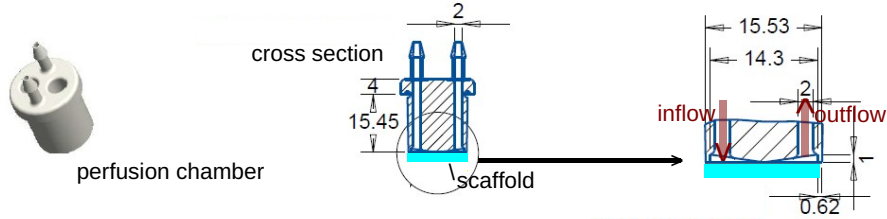
Continuous settings have the advantage of enabling mathematically well-founded qualitative analyses and fast, efficient numerical simulations. This usually makes up for them typically including less details than their discrete or hybrid counterparts. The vast majority of continuous approaches involve reaction-diffusion-(transport) equations (RD(T)Es) to describe the dynamics of *macroscopic* cell densities interacting with soluble or insoluble extracellular components and leading to tactic cell migration. There is a vast literature concerning such systems; we refer to the reviews in [11] and [40], and e.g., to [70, 71, 76, 77] for the analysis of models paying enhanced attention to effects of heterogeneous tissues on cell migratory and proliferative behavior. Nonlocal RDTE models also attach importance to phenomena taking place at longer range than just at the very location of a cell; this is particularly relevant for high cell densities and for more detailed descriptions cell-cell and/or cell-tissue interactions. We refer to [16] for a review of such models; in [23] we established rigorous relationships with cell-cell and cell-tissue adhesion models involving spatial nonlocality. RDTE models for tissue regeneration taking into account the evolution of cell populations with various phenotypes are rather rare; some of them [6, 14, 15, 30] account for biochemical influences, others also for mechanical ones see e.g. [3, 33, 63, 65]. We are, however, not aware of any formulations capturing in this context the topography of underlying tissue - the less so, as far as meniscus regeneration is concerned. The works [7, 8] provide a rather detailed description of anisotropic tissue-like structures populated with cells whose migratory behavior is influenced by such surroundings and their mechanics, but in the setting of a biphasic theory and the fibre orientation distribution is thereby not assessed statistically from experiments.

Multiphase models are another continuous approach, where cell populations are seen as components of a mixture also containing fluid(s) in which chemical cues are dissolved and/or tissue. Mass and momentum balance are typically required for each of the involved phases, supplemented with appropriate closure laws, see e.g. [4, 9, 44, 45]; the review [39] of multiphase cartilage mechanical modeling explicitly excludes descriptions of cell behavior involved in the process. The advantage of mixture-based approaches is their ability to pay enhanced attention to biomechanics ([9]), however their rigorous mathematical analysis is challenging and has scarcely been addressed, mainly just in 1D, and for substantially simplified settings leading to smaller RDTE systems (see e.g., [26] and references therein). Connections between multiphase models and RDTE systems for (tumor) cell migration and spread in the extracellular matrix have been done in [37] (1D case) and [42] (higher dimensions, more complex setting). Multiphase models are commonly macroscopic, however some works within this framework also addressed multiscality [35, 56], see also the review [12] and references therein.

Mesoscale models involve cell density distributions depending on time, position, cell velocity, and so-called activity variables in the kinetic theory of active particles framework [10]. They are intermediates between single cell and macroscopic dynamics and feature kinetic transport equations (KTEs), with integral terms describing velocity innovations as consequences of cell reorientations, along with chemo- and haptotactic bias. Such models are able to incorporate detailed information about the anisotropy of fibrous tissue surrounding the cells and capture effects of such topography on the motility and phenotypic switch of cellular matter. Adequate upscaling and moment closure procedures lead again, for the cell



(a) Setup for array of perfusions chambers (pressure caps)



(b) Geometry of the perfusion chamber (lengths in [mm])



(c) Scaffold dimensions (lengths in [mm])

Figure 1: Sketch of in-vitro experiment

populations of interest, to macroscopic RDTEs carrying in their motility (myopic diffusion and taxis) and source terms (proliferation/decay/phenotypic switch) the said influences of tissue structure and chemoattractants and/or -repellents. A variety of such models have been developed and investigated [18, 20, 21, 24, 25, 41, 57, 75], primarily in connection to glioma invasion in brain tissue, where patient-specific anisotropy seems to be essential for the spread of cancer cells. Thereby, the recent works [20, 21, 75] also proposed some ways to include biomechanics in the description of cell and tissue dynamics. The cell motility terms of the obtained macroscopic PDEs involve flux-limited diffusion and taxis. While the vast majority of passages from KTEs to RDTEs is informal, we introduced in [75] a novel method to derive a rigorous macroscopic limit. All mentioned model types can accommodate multiscale either through adequate couplings of ODEs with PDEs as e.g., in [46, 71], or by some of the kinetic variables being obtained on another modeling level, as in [20, 21, 24, 25, 41].

The paper is organized as follows: Section 2 is dedicated to obtaining the macroscopic model comprising effective RDTEs for the dynamics of involved cell populations (stem cells and their differentiated counterparts), which are then coupled to fluid mechanics and deformations of scaffold and newly generated tissue, but also to the equations for the evolution of hyaluron (which impregnates the scaffold), differentiation factor, and newly formed tissue. Section 3 provides information about the performed experiments and the data processing. In Section 4 we perform numerical simulations of the model. Finally, Section 5 contains a discussion of the results and an outlook.

2 Mathematical modeling

This section is concerned with the detailed derivation of a new mathematical model for the major biological processes that characterize the cell colonization in a scaffold for meniscus regeneration. We start by addressing the connection between the micro-, meso- and macroscopic scales and then extend the model by mechanical effects that stem from the surrounding perfusion chamber. Fig. 1 shows the experimental setup.

2.1 A multiscale approach connecting subcellular and population levels

We consider a first model for the dynamics of human mesenchymal stem cells (hMSCs) differentiating into and interacting with chondrocytes, under chemical, topological, and mechanical environmental influences. Chondrocytes produce ECM and hyaluron, also uptaking the latter. The cells migrate, differentiate, and proliferate inside an artificial scaffold with given topology, which does not infer resorption by the cells and whose fibers are impregnated with hyaluron, that acts as a (nondiffusing) chemoattractant for the hMSCs. The differentiation of hMSCs to chondrocytes and the phenotype preservation of the latter are induced and sustained by a differentiation medium. We start at the microscopic level of single cells and therewith associated receptor binding dynamics, then pass through the mesoscale of cell distribution functions, and obtain by a parabolic upscaling effective equations for the dynamics of macroscopic population densities. The method follows closely that in [18–20].

Microscopic, subcellular scale. We account for binding of hMSC receptors to their ligands available in the extracellular space. Here we focus on interactions with the chemoattractant (hyaluron) and with ECM and provide on this level less details for the exchange of chondrocytes with their environment.

Let y_1 denote the amount of hMSC receptors occupied with hyaluron (of density h and reference density H) and y_2 be the amount of hMSC receptors bound to ECM (of density τ and reference density K). Simple receptor binding kinetics then takes the form

$$\begin{aligned} (R_0 - y_1 - y_2) + \frac{h}{H} \frac{k_1^+}{k_1^-} y_1 \\ (R_0 - y_1 - y_2) + \frac{\tau}{K} \frac{k_2^+}{k_2^-} y_2, \end{aligned}$$

where R_0 represents the total amount of bound receptors on an hMSC membrane; we assume R_0 to be constant. Then we get the ODE system

$$\begin{aligned} \dot{y}_1 &= k_1^+ \frac{h}{H} (R_0 - y_1 - y_2) - k_1^- y_1 \\ \dot{y}_2 &= k_2^+ \frac{\tau}{K} (R_0 - y_1 - y_2) - k_2^- y_2, \end{aligned}$$

with k_j^+ and k_j^- denoting attachment and respectively detachment rates of hMSC to hyaluron ($j = 1$) and ECM ($j = 2$). For simplicity we assume $k_1^- = k_2^- =: k^-$. Let us denote $y := y_1 + y_2$. Then we get

$$\dot{y} = \left(k_1^+ \frac{h}{H} + k_2^+ \frac{\tau}{K} \right) (R_0 - y) - k^- y \quad (2.1)$$

Rescaling $y/R_0 \rightsquigarrow y \in (0, 1)$ further simplifies the notation. Since receptor binding is very fast compared to the overall dynamics of cell migration and proliferation, we assume it to quickly reach the equilibrium and only deal with the steady-state of the above equation:

$$y^* = \frac{k_1^+ \frac{h}{H} + k_2^+ \frac{\tau}{K}}{k_1^+ \frac{h}{H} + k_2^+ \frac{\tau}{K} + k^-}.$$

We denote by $z := y^* - y$ the (very small) deviation of y from y^* and proceed as in [18–20, 24, 25] to obtain from (2.1)

$$\dot{z} = -zB(h, \tau) + \frac{k^-}{(B(h, \tau))^2} v \cdot \nabla_x B(h, \tau) := G(z, h, \tau),$$

with $B(h, \tau) := k_1^+ \frac{h}{H} + k_2^+ \frac{\tau}{K} + k^-$.

Mesosopic level. The dynamics of cell density distributions for hMSCs and chondrocytes is described by way of kinetic transport equations. Let $p_1(t, x, v, z)$ denote the density of hMSCs sharing at time $t > 0$ and position $x \in \mathbb{R}^n$ the velocity regime $v \in V_1 = s_1 \mathbb{S}^{n-1}$ and the deviation $z \in Z = (y^* - 1, y^*)$ from the equilibrium receptor binding state. Likewise, $p_2(t, x, v)$ represents the density of chondrocytes with velocity $v \in V_2 = s_2 \mathbb{S}^{n-1}$. The positive constants s_1 and s_2 are the speeds of hMSCs and chondrocytes, respectively. The KTEs for p_1 and p_2 then write

$$\partial_t p_1 + \nabla_x \cdot (v p_1) + \partial_z (G(z, h, \tau) p_1) = \mathcal{L}_1[\lambda_1(z)] p_1 + (\text{de})\text{differentiation \& proliferation} \quad (2.2)$$

$$\partial_t p_2 + \nabla_x \cdot (v p_2) = \mathcal{L}_2[\lambda_2] p_2 + (\text{de})\text{differentiation.} \quad (2.3)$$

The first terms on the right hand sides of (2.2) and (2.3) characterize the reorientation of hMSCs and chondrocytes, respectively. Concretely, choose for the turning operators

$$\mathcal{L}_1[\lambda_1(z)]p_1(t, x, v, z) := -\lambda_1(z)p_1(t, x, v, z) + \lambda_1(z) \int_{V_1} K_1(x, v)p(t, x, v', z)dv' \quad (2.4)$$

$$\mathcal{L}_2[\lambda_2]p_2(t, x, v) := -\lambda_2 p_2(t, x, v) + \lambda_2 \int_{V_2} K_2(x, v)p_2(t, x, v')dv', \quad (2.5)$$

with the turning rates $\lambda_1(z) = \lambda_{10} - \lambda_{11}z \geq 0$ as in [18, 19, 24, 25], where $\lambda_{10}, \lambda_{11} > 0$ are constants and $\lambda_2 > 0$ is a constant, too. For the turning kernels we take into account (as in [18, 19, 24, 25, 57]) the anisotropy of the scaffold fibers and choose $K_j(x, v) := q(x, \hat{v})/\omega_j$ ($j = 1, 2$), where $\hat{v} = \frac{v}{|v|}$ and $q(x, \theta)$ with $\theta \in \mathbb{S}^{n-1}$ is the orientational distribution of the scaffold fibers, normalised by $\omega_j = s_j^{n-1}$. We assume the tissue to be undirected, hence $q(x, \theta) = q(x, -\theta)$ for all x in \mathbb{R}^n and $\theta \in \mathbb{S}^{n-1}$. We introduce the notations

$$\begin{aligned} \mathbb{E}_q(x) &= \int_{\mathbb{S}^{n-1}} \theta q(x, \theta) d\theta \quad (\text{observe that } \mathbb{E}_q = 0) \\ \mathbb{V}_q(x) &= \int_{\mathbb{S}^{n-1}} (\theta - \mathbb{E}_q) \otimes (\theta - \mathbb{E}_q) q(x, \theta) d\theta. \end{aligned}$$

The turning operators in (2.4), (2.5) take the form

$$\mathcal{L}_j[\lambda_j]p_j := \lambda_j \left(\frac{q(x, \hat{v})}{\omega_j} \int_{V_j} p_j dv - p_j(v) \right) \quad (j = 1, 2).$$

We denote by $c_1(t, x) := \iint_{V_1 \times Z} p_1(t, x, v, z) d(v, z)$ and $c_2(t, x) := \int_{V_2} p_2(t, x, v) dv$ the macroscopic densities of hMSCs and chondrocytes, respectively.

The source terms on the right hand sides in (2.2) and (2.3) describe proliferation and growth/decay due to differentiation of hMSCs into chondrocytes and dedifferentiation of the latter. Such processes need a substantially longer time to happen when compared to cell migration, therefore will require a rescaling by a sufficiently small factor ε^2 . We assume that the cell phenotype is neither determined by the cell direction nor by the orientation of fibers in the scaffold, but only depends on macroscopic quantities in the extracellular space. Then (2.2) and (2.3) take the form

$$\partial_t p_1 + \nabla_x \cdot (vp_1) + \partial_z(G(z, h, \tau)p_1) = \mathcal{L}_1[\lambda_1(z)]p_1 + \varepsilon^2 \left(-\alpha_1(\chi, S)p_1 + \alpha_2(\chi, S)p_2 + \beta p_1 \left(1 - \frac{c_1}{C_1^*} - \frac{c_2}{C_2^*} \right) \right) \quad (2.6)$$

$$\partial_t p_2 + \nabla_x \cdot (vp_2) = \mathcal{L}_2[\lambda_2]p_2 + \varepsilon^2 (\alpha_1(\chi, S)p_1 - \alpha_2(\chi, S)p_2), \quad (2.7)$$

where C_j^* denotes the carrying capacity of the cell population j ($j = 1, 2$), $\beta > 0$ is the constant growth rate of hMSCs, and $\alpha_1(\chi, S), \alpha_2(\chi, S)$ represent the rates of differentiation of hMSCs into chondrocytes and dedifferentiation of the latter, respectively. The functions α_j depend on the concentration χ of the differentiation medium. Moreover, mechanical and chemical effects influence cell de(differentiation) [5, 27, 38, 43] and can be included upon letting α_j depend on concentrations of such chemicals and a stress-related quantity S [64], e.g. $S = \frac{\sigma}{\mu_1} + \frac{\vartheta}{\mu_2}$, with σ and ϑ denoting known maximum shear stress and interstitial fluid speed, respectively, and $\mu_j > 0$ ($j = 1, 2$) being constants [3, 36].

The high dimensionality of this system would require expensive numerical simulations, therefore we deduce in the next subsection a system of macroscopic equations for the dynamics of the two cell populations. An effective macroscopic system is also more conducive for assessing the relevant behavior of hMSCs and chondrocytes in interaction with hyaluron and (newly produced) ECM.

Let us introduce the following moments of p_1 with respect to the 'activity' variable z and velocity v :

$$m(t, x, v) := \int_Z p_1(t, x, v, z) dz, \quad m^z(t, x, v) := \int_Z z p_1(t, x, v, z) dz, \quad M^z(t, x) := \int_{V_1} m^z(t, x, v) dv.$$

Due to the fact that z is very small we will neglect moments of p_1 w.r.t. z for higher orders. This will ensure the subsequent informal moment closure.

Upscaling and macroscopic level. We perform a parabolic scaling of the time and space variables: $t \rightsquigarrow \varepsilon^2 t$ and $x \rightsquigarrow \varepsilon x$. Applying this to (2.6), (2.7) leads to

$$\varepsilon^2 \partial_t p_1 + \varepsilon \nabla_x \cdot (vp_1) + \partial_z \left(\left(-zB(h, \tau) + \varepsilon \frac{k^-}{(B(h, \tau))^2} v \cdot \nabla_x B(h, \tau) \right) p_1 \right)$$

$$= \mathcal{L}_1[\lambda_1(z)]p_1 + \varepsilon^2 \left(-\alpha_1(\chi, S)p_1 + \alpha_2(\chi, S)p_2 + \beta p_1 \left(1 - \frac{c_1}{C_1^*} - \frac{c_2}{C_2^*} \right) \right) \quad (2.8)$$

$$\varepsilon^2 \partial_t p_2 + \varepsilon \nabla_x \cdot (vp_2) = \mathcal{L}_2[\lambda_2]p_2 + \varepsilon^2 (\alpha_1(\chi, S)p_1 - \alpha_2(\chi, S)p_2). \quad (2.9)$$

We assume p_1 to be compactly supported in the phase space $\mathbb{R}^n \times V_1 \times Z$. Integrating (2.8) w.r.t. z gives

$$\begin{aligned} \varepsilon^2 \partial_t m + \varepsilon \nabla_x \cdot (vm) &= -\lambda_{10} \left(m - \frac{q}{\omega_1} c_1 \right) + \lambda_{11} \left(m^z - \frac{q}{\omega_1} M^z \right) \\ &\quad + \varepsilon^2 \left(-\alpha_1(\chi, S)m + \alpha_2(\chi, S)p_2 + \beta m \left(1 - \frac{c_1}{C_1^*} - \frac{c_2}{C_2^*} \right) \right). \end{aligned} \quad (2.10)$$

Now multiply (2.8) by z and integrate w.r.t. z to get

$$\begin{aligned} \varepsilon^2 \partial_t m^z + \varepsilon \nabla_x \cdot (vm^z) + m^z B(h, \tau) - \varepsilon \frac{k^-}{(B(h, \tau))^2} v \cdot \nabla_x B(h, \tau) m &= -\lambda_{10} \left(m^z - \frac{q}{\omega_1} M^z \right) - \varepsilon^2 \alpha_1(\chi, S) m^z \\ &\quad + \varepsilon^2 \alpha_2(\chi, S) p_2 (y^* - 2) + \varepsilon^2 \beta m^z \left(1 - \frac{c_1}{C_1^*} - \frac{c_2}{C_2^*} \right). \end{aligned} \quad (2.11)$$

We perform Hilbert expansions of the p_1 -moments and of p_2 and c_2 :

$$m = \sum_{j=0}^{\infty} \varepsilon^j m_j, \quad m^z = \sum_{j=0}^{\infty} \varepsilon^j m_j^z, \quad c_1 = \sum_{j=0}^{\infty} \varepsilon^j c_{1j}, \quad M^z = \sum_{j=0}^{\infty} \varepsilon^j M_j^z, \quad p_2 = \sum_{j=0}^{\infty} \varepsilon^j p_{2j}, \quad c_2 = \sum_{j=0}^{\infty} \varepsilon^j c_{2j}.$$

Equating powers of ε in (2.9), (2.10), (2.11) we get

ε^0 :

$$0 = \lambda_2 \left(\frac{q}{\omega_2} c_{20} - p_{20} \right) \quad (2.12)$$

$$0 = -\lambda_{10} \left(m_0 - \frac{q}{\omega_1} c_{10} \right) + \lambda_{11} \left(m_0^z - \frac{q}{\omega_1} M_0^z \right) \quad (2.13)$$

$$m_0^z B(h, \tau) = -\lambda_{10} \left(m_0^z - \frac{q}{\omega_1} M_0^z \right) \quad (2.14)$$

ε^1 :

$$\nabla_x \cdot (vp_{20}) = \lambda_2 \left(\frac{q}{\omega_2} c_{21} - p_{21} \right)$$

$$\nabla_x \cdot (vm_0) = -\lambda_{10} \left(m_1 - \frac{q}{\omega_1} c_{11} \right) + \lambda_{11} \left(m_1^z - \frac{q}{\omega_1} M_1^z \right) \quad (2.15)$$

$$\nabla_x \cdot (vm_0^z) + m_1^z B(h, \tau) - \frac{k^-}{(B(h, \tau))^2} v \cdot \nabla_x B(h, \tau) m_0 = -\lambda_{10} \left(m_1^z - \frac{q}{\omega_1} M_1^z \right) \quad (2.16)$$

ε^2 (from (2.9), (2.10)):

$$\partial_t p_{20} + \nabla_x \cdot (vp_{21}) = \lambda_2 \left(\frac{q}{\omega_2} c_{22} - p_{22} \right) + \alpha_1(\chi, S)p_{10} - \alpha_2(\chi, S)p_{20}$$

$$\begin{aligned} \partial_t m_0 + \nabla_x \cdot (vm_1) &= -\lambda_{10} \left(m_2 - \frac{q}{\omega_1} c_{12} \right) + \lambda_{11} \left(m_2^z - \frac{q}{\omega_1} M_2^z \right) - \alpha_1(\chi, S)m_0 + \alpha_2(\chi, S)p_{20} \\ &\quad + \beta m_0 \left(1 - \frac{c_{10}}{C_1^*} - \frac{c_{20}}{C_2^*} \right). \end{aligned}$$

Integrate (2.14) w.r.t. v to obtain $M_0^z = 0$. Substitute this in (2.14) to follow $m_0^z = 0$. From (2.13) and (2.12) follows

$$m_0 = \frac{q}{\omega_1} c_{10}, \quad p_{20} = \frac{q}{\omega_2} c_{20}. \quad (2.17)$$

Integrating (2.16) w.r.t. v leads to $M_1^z = 0$. Then from (2.16) we obtain

$$m_1^z = \frac{k^-}{B(h, \tau)^2 (B(h, \tau) + \lambda_{10})} v \cdot \nabla_x B(h, \tau) \frac{q}{\omega_1} c_{10}. \quad (2.18)$$

Now apply the operator $\mathcal{L}_1[\lambda_{10}]$ to $m_1(t, x, v) = \int_Z p_{11}(t, x, v, z) dz$:

$$\begin{aligned}\mathcal{L}_1[\lambda_{10}]m_1 &= \lambda_{10} \left(\frac{q}{\omega_1} c_{11} - m_1 \right) \\ &= \nabla_x \cdot (vm_0) - \lambda_{11} m_1^z \quad (\text{due to (2.15)}).\end{aligned}$$

The compact Hilbert-Schmidt operator on the weighted space $L^2_{\frac{q}{\omega_1}}(V_1) := \{w \in L^2(V_1) : \int_{V_1} w^2 \frac{dv}{\omega_1} < \infty\}$ has kernel $\left\langle \frac{q}{\omega_1} \right\rangle := \text{span}\left(\frac{q}{\omega_1}\right)$, thus its pseudo-inverse can be determined on $\left\langle \frac{q}{\omega_1} \right\rangle^\perp$. We obtain (for more details refer e.g., to [24, 54]):

$$m_1 = -\frac{1}{\lambda_{10}} (\nabla_x \cdot (vm_0) - \lambda_{11} m_1^z), \quad \text{thus } c_{11} = 0. \quad (2.19)$$

Analogously,

$$p_{21} = -\frac{1}{\lambda_2} (\nabla_x \cdot (vp_{20})), \quad \text{thus } c_{21} = 0. \quad (2.20)$$

Now integrate the ε^2 -equations w.r.t. v to obtain

$$\partial_t c_{10} + \nabla_x \cdot \int_{V_1} vm_1 dv = -\alpha_1(\chi, S)c_{10} + \alpha_2(\chi, S) \frac{\omega_1}{\omega_2} c_{20} + \beta c_{10} \left(1 - \frac{c_{10}}{C_1^*} - \frac{c_{20}}{C_2^*} \right) \quad (2.21)$$

$$\partial_t c_{20} + \nabla_x \cdot \int_{V_2} vp_{21} dv = \alpha_1(\chi, S) \frac{\omega_2}{\omega_1} c_{10} - \alpha_2(\chi, S)c_{20}. \quad (2.22)$$

In virtue of (2.19) we evaluate

$$\begin{aligned}\nabla_x \cdot \int_{V_1} vm_1 &= -\nabla \nabla : (\mathbb{D}_1 c_{10}) + \nabla \cdot \left(\frac{k^- \lambda_{11}}{B(h, \tau)^2 (B(h, \tau) + \lambda_{10})} \mathbb{D}_1 \nabla B(h, \tau) c_{10} \right) \\ \nabla_x \cdot \int_{V_2} vp_{21} &= -\nabla \nabla : (\mathbb{D}_2 c_{20}),\end{aligned}$$

with

$$\mathbb{D}_1(x) = \frac{1}{\lambda_{10}} \int_{V_1} v \otimes v \frac{q(x, \hat{v})}{\omega_1} dv = \frac{s_1^2}{\lambda_{10}} \int_{\mathbb{S}^{n-1}} \theta \otimes \theta q(x, \theta), \quad (2.23)$$

$$\mathbb{D}_2(x) = \frac{1}{\lambda_2} \int_{V_2} v \otimes v \frac{q(x, \hat{v})}{\omega_2} dv = \frac{\lambda_{10}}{\lambda_2} \left(\frac{s_2}{s_1} \right)^2 \mathbb{D}_1(x). \quad (2.24)$$

Plugging these into (2.21), (2.22) and neglecting higher order terms in the Hilbert expansions of c_1 and c_2 (see also (2.19), (2.20)) we obtain the macroscopic reaction-diffusion-taxis equations (RDTEs)

$$\begin{aligned}\partial_t c_1 - \nabla \nabla : (\mathbb{D}_1 c_1) + \nabla \cdot \left(\frac{k^- \lambda_{11}}{B(h, \tau)^2 (B(h, \tau) + \lambda_{10})} \mathbb{D}_1 \nabla B(h, \tau) c_1 \right) &= -\alpha_1(\chi, S)c_1 + \alpha_2(\chi, S) \frac{\omega_1}{\omega_2} c_2 \\ &\quad + \beta c_1 \left(1 - \frac{c_1}{C_1^*} - \frac{c_2}{C_2^*} \right) \quad (2.25)\end{aligned}$$

$$\partial_t c_2 - \nabla \nabla : (\mathbb{D}_2 c_2) = \alpha_1(\chi, S) \frac{\omega_2}{\omega_1} c_1 - \alpha_2(\chi, S)c_2. \quad (2.26)$$

Thereby, $\nabla \nabla : (\mathbb{D}c) = \nabla \cdot (\nabla \cdot \mathbb{D}c + \mathbb{D}\nabla c)$ represents myopic diffusion; the Fickian diffusion with tensor $\mathbb{D} \in \mathbb{R}^{n \times n}$ infers a drift correction with convection velocity $\nabla \cdot \mathbb{D}$.

We supplement the above RDTEs with the dynamics of differentiation medium with concentration χ

$$\partial_t \chi = D_\chi \Delta \chi - a_\chi (c_1 + c_2) \chi \quad (2.27)$$

representing diffusion and uptake by both cell phenotypes along with those for hyaluron concentration h and ECM density τ , none of which is supposed to diffuse:

$$\partial_t h = -\gamma_1 h c_1 - \gamma_2 h c_2 + \frac{c_2}{1 + c_2} \quad (2.28)$$

$$\partial_t \tau = -\delta c_1 \tau + c_2, \quad (2.29)$$

with the source terms on the right hand side characterizing production, degradation, and uptake of h and τ due to c_1 and c_2 .

Thus far we dealt with $x \in \mathbb{R}^n$; however, we should actually consider a bounded region $\Omega_p \subset \mathbb{R}^n$ in which cells, ECM, and hyaluron are evolving.¹ This raises the need for boundary conditions, which can be obtained as e.g. in [62], see also [18, 20] for similar deductions. Hence, we supplement system (2.25)-(2.29) with no-flux boundary conditions

$$\left(\mathbb{D}_1 \nabla c_1 + \left(\nabla \cdot \mathbb{D}_1 - \frac{k^- \lambda_{11}}{B(h, \tau)^2 (B(h, \tau) + \lambda_{10})} \mathbb{D}_1 \nabla B(h, \tau) \right) c_1 \right) \cdot \nu = 0 \quad \text{on } \partial \Omega_p \quad (2.30)$$

$$(\nabla \cdot \mathbb{D}_2 c_2 + \mathbb{D}_2 \nabla c_2) \cdot \nu = 0 \quad \text{on } \partial \Omega_p. \quad (2.31)$$

We also consider a no-flux boundary condition for χ :

$$\nabla \chi \cdot \nu = 0 \quad \text{on } \partial \Omega_p. \quad (2.32)$$

For the initial conditions we consider h to be uniformly distributed in space: $h_0(x) = \tilde{h}_0 \frac{1}{|\Omega_p|} \mathbb{1}_{\Omega_p}(x)$, with \tilde{h}_0 a given constant. The initial densities $c_{1,0}$ and $c_{2,0}$ of hMSCs and chondrocytes, respectively, are considered to be Gaussians, as the cells are placed at the center of the upper scaffold interface, from where they spread. We take $\tau(0, x) = 0$, as there is initially no newly formed ECM. The differentiation medium is provided at several different times during the experiment, each time the same overall quantity, which is supposed to quickly diffuse within the whole domain Ω_p , thus we consider it to be uniformly distributed: $\chi(t \in T_\chi, x) = \chi_0 \frac{1}{|\Omega_p|} \mathbb{1}_{\Omega_p}(x)$, where $T_\chi = \{0, 2, 3, 6, 9, 12, 15, 18, 21, 24\}$ is the set containing the time points (in days) where the available differentiation medium is substituted by a new one, with concentration χ_0 .

2.2 Including mechanical effects

The cells migrate, proliferate, and (de)differentiate within an articial scaffold integrated in a 3D printed perfusion chamber which is embedded in a bioreactor². As mentioned in above, mechanical stress is an important factor leading to cell (de)differentiation. To account for it, the bioreactor is endowed with an alternating fluid flowing through the perfusion chamber tubes and releasing the pressure.

Thus, the previously obtained macroscopic model for the dynamics of cells, hyaluron, and newly produced ECM is to be supplemented with fluid dynamics and therewith induced deformations of the scaffold. These, in turn, will affect the evolution of c_1 , c_2 , h , and τ , the coupling being realized by way of the (de)differentiation rates α_1 and α_2 which appear on the right hand sides of (2.25) and (2.26). We proceed as in [32] and consider the tissue (ECM and scaffold) as a poroelastic medium which we model by the Biot equations (see e.g. [2])

$$\rho_s \partial_{tt} \boldsymbol{\eta}_p - \nabla \cdot \boldsymbol{\sigma}_p(\boldsymbol{\eta}_p, p_p) = 0, \quad (2.33a)$$

$$\partial_t \left(\frac{1}{M} p_p + \nabla \cdot (\alpha \boldsymbol{\eta}_p) \right) + \nabla \cdot \mathbf{u}_p = 0, \quad (2.33b)$$

with the displacement field $\boldsymbol{\eta}_p(t, x)$ and the pressure $p_p(t, x)$ in a domain $\Omega_p \subset \mathbb{R}^n$, with additional boundary and initial conditions. Here, ρ_s stands for the solid phase density, while M and α are Biot's modulus and coefficient, respectively. The stress tensor $\boldsymbol{\sigma}_p$ is given by

$$\boldsymbol{\sigma}_p(\boldsymbol{\eta}_p, p_p) = \boldsymbol{\sigma}_e(\boldsymbol{\eta}_p) - \alpha p_p I, \quad \text{and} \quad \boldsymbol{\sigma}_e(\boldsymbol{\eta}_p) = \lambda_p (\nabla \cdot \boldsymbol{\eta}_p) I + 2\mu_p D(\boldsymbol{\eta}_p), \quad (2.34)$$

with λ_p and μ_p being the Lamé parameters, whereas the fluid flux satisfies Darcy's law

$$\mathbf{u}_p = -\mathbb{K}(\nabla p - \rho_f \mathbf{g})/\mu, \quad (2.35)$$

with permeability matrix \mathbb{K} , fluid phase density ρ_f , and viscosity μ . Additionally, a Stokes flow is considered:

$$\rho_f \partial_t \mathbf{u}_f - \nabla \cdot \boldsymbol{\sigma}_f(\mathbf{u}_f, p_f) = 0, \quad \text{and} \quad \nabla \cdot \mathbf{u}_f = 0, \quad \text{in } \Omega_f, \quad (2.36)$$

¹Subsequently Ω_p will be a bounded and convex subdomain of a domain $\Omega \subset \mathbb{R}^n$ with sufficiently regular boundary $\partial \Omega$.

²Experimental setup designed and implemented at DITF Denkendorf by M. Dauner, M. Doser, C. Linti, and A. Ott

for the fluid stress tensor given by $\boldsymbol{\sigma}_f(\mathbf{u}_f, p_f) := -p_f I + 2\mu D(\mathbf{u}_f)$, with $D(\mathbf{u}_f) = \frac{1}{2}(\nabla \mathbf{u}_f + \nabla \mathbf{u}_f^T)$ and where ρ_f stands for the fluid phase density.

The cells and the deformation of tissue evolve in Ω_p , while Ω_f is the domain occupied by the fluid. It holds that $\Omega = \Omega_p \cup \Omega_f$ and we denote by \mathbf{n}_f the outward unit normal vector to the boundaries $\Gamma_f = \Gamma_I \cup \Gamma_{f,W} \cup \Gamma_{in} \cup \Gamma_{out}$, where Γ_I represents the interface between Ω_f and Ω_p , $\Gamma_{f,W}$ represents the wall boundaries of Ω_f , and Γ_{in} , Γ_{out} are the inflow and outflow boundaries, respectively.

The boundary conditions for the fluid are

$$\begin{aligned} \mathbf{u}_f &= 0 \text{ on } \Gamma_{f,W}, \\ \boldsymbol{\sigma}_f \mathbf{n}_f &= -p_{in}(t) \mathbf{n}_f \text{ and } \mathbf{u}_f \times \mathbf{n}_f = 0 \text{ on } \Gamma_{in}, \\ \boldsymbol{\sigma}_f \mathbf{n}_f &= 0 \text{ on } \Gamma_{out}. \end{aligned}$$

The pressure boundary condition at the inflow is set to $p_{in}(t) = p_{max} \sin(\pi t)$.

Likewise, we denote $\Gamma_p := \Gamma_{p,W} \cup \Gamma_I$, where $\Gamma_{p,W}$ represents the 'wall boundary' of the region Ω_p . We require

$$p_p = 0 \text{ and } \boldsymbol{\eta}_p = 0 \text{ on } \Gamma_{p,W}.$$

At the interface Γ_I we prescribe the following conditions:

- mass conservation:

$$\mathbf{u}_f \cdot \mathbf{n}_f + (\partial_t \eta_p + \mathbf{u}_p) \cdot \mathbf{n}_p = 0. \quad (2.37)$$

- balance of stresses:

$$\begin{aligned} -(\boldsymbol{\sigma}_f \mathbf{n}_f) \cdot \mathbf{n}_f &= (p_f - 2\mu D(\mathbf{u}_f)) \mathbf{n}_f \cdot \mathbf{n}_f = p_p, \\ \boldsymbol{\sigma}_f \cdot \mathbf{n}_f + \boldsymbol{\sigma}_p \cdot \mathbf{n}_p &= (2\mu_f D(\mathbf{u}_f) - p_f I) \cdot \mathbf{n}_f + (\lambda_p \nabla \cdot \boldsymbol{\eta} + 2\mu_p D(\boldsymbol{\eta}) - \alpha p_p) \cdot \mathbf{n}_p = 0. \end{aligned} \quad (2.38)$$

- the Beavers-Joseph-Saffman (BJS) condition modeling slip with friction:

$$-(\boldsymbol{\sigma}_f \mathbf{n}_f)_T = \underbrace{\mu_f \alpha \mathbb{K}^{-1/2}}_{\alpha_{BJS}} (\mathbf{u}_f - \partial_t \boldsymbol{\eta}_p)_T, \quad (2.39)$$

where α_{BJS} is the slip rate coefficient and $(\cdot)_T$ is the tangential component.

For the coupling via the rates α_1 and α_2 we propose an approach inspired by [3, 64], where the mechanical stimulus S is defined as a linear combination between a strain-related quantity and the fluid velocity. The authors showed that S would favor chondrocyte differentiation and ECM synthesis if it got between two values, S_{min} and S_{max} . We thus propose a mapping between $\boldsymbol{\sigma}_p$ and α_1 , α_2 , which thus become dependent on time, space, and on the stress. Such dependency is shown in Figure 2.

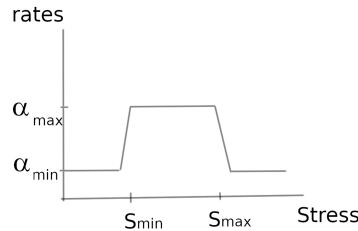


Figure 2: Shape of mapping connecting mechanical stimulus S with (de)differentiation rates

3 Experimental data

This section summarizes the experimental work that has been carried out so far, starting with the fabrication of nonwoven scaffolds and then proceeding with image analysis and a biomechanical characterization.

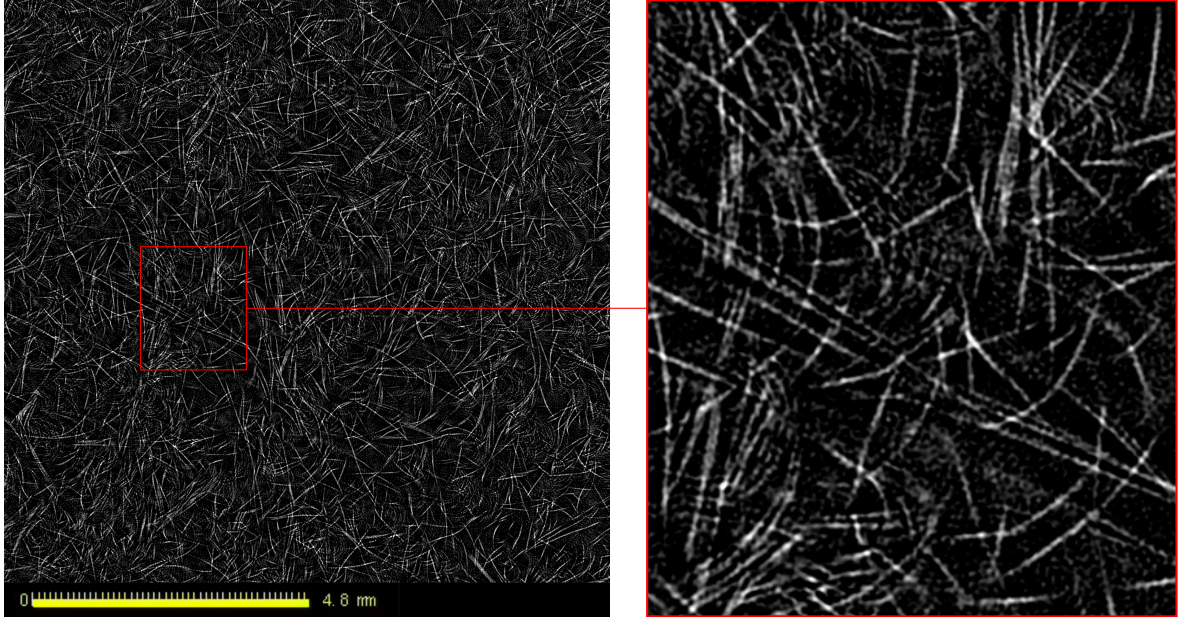


Figure 3: Sectional image of the CT scan of sample 1 (left). The area marked by a red box is magnified 5 times (right) to enhance the visibility of the fiber structure.

3.1 Scaffold fabrication

A PET (polyethylene terephthalate) multifilament was extruded and stretched, the resulting diameter of the individual filament was $17\mu\text{m}$. The filaments were cut to fibers of about 60mm length and the fibers were thermally treated in a drying oven to avoid shrinkage in the subsequent process steps. A non-woven fiber web was formed from these fibers with a carding machine by winding a defined number of pile layers up to the desired weight. The fiber web was then mechanically solidified by a needle machine. In order to achieve a predetermined porosity, the resulting needle felt was passed through a defined gap between two heated calender rolls and the required fleece thickness was thermally set. Thus, non-woven scaffolds with a thickness of about 1.8mm and a slightly different porosity were generated: one with a weight of $267 - 292\text{g}/\text{m}^2$ (LW, 88% porosity) and one with $400 - 420\text{g}/\text{m}^2$ (HW, 85% porosity).

3.2 Imaging analysis of simple scaffolds

Six scaffold samples were scanned by micro computed tomography using a Skyscan1172 device. A source voltage of 40 kV and a current of $250\mu\text{A}$ were used. The angular step width in the rotation was 0.3 degrees resulting in 1202 projection images. The voxel spacing is $3.98\mu\text{m}$.

We cropped the images such that the cuboid field of view is entirely inside the cylindrical specimen (approx. $2600 \times 2600 \times 300$ voxels). A sectional image is shown in Figure 3. In a preprocessing step, we smoothed the CT image with a Gaussian filter (filter mask size: $7 \times 7 \times 7$, $\sigma = 6.0$, reflective edge treatment) to remove noise while preserving edges. These parameters were chosen according to the fiber diameter which corresponds to approximately $r \approx 6$ voxels.

To achieve a coarse segmentation of the fiber system, we deployed Otsu's thresholding method [55] with a factor of 1.25. For further refinement, we applied a median filter (filter mask size: $3 \times 3 \times 3$, reflective edge treatment), then a morphological closing operation (structuring element size: $5 \times 5 \times 5$), and, subsequently, the median filter again. Lastly, we removed connected components of sizes smaller than 50 voxels because these are likely too small to constitute single fibers.

For each fiber voxel, we estimated the fiber orientation with the Hessian matrix of the grey value image [22, 52]. The approach is based on the idea that the fiber direction is aligned with the direction of minimal curvature. Therefore, the eigenvector belonging to the smallest eigenvalue of the Hessian is used as the fiber direction estimate. For computing the Hessian, we used $\sigma = 3$, which equals the fibre radius, since this choice has been shown to be optimal in [61, 74].

In the next step, the fiber direction in the typical fiber point (in Palm sense, see [17]) is modelled by an angular central Gaussian (ACG) distribution. The density of this distribution model on the unit sphere

	A_{11}	A_{12}	A_{13}	A_{22}	A_{23}	A_{33}
Sample 0	1.697	0.023	-0.028	0.873	-0.031	0.324
Sample 1	1.687	0.003	0.064	0.914	-0.007	0.399
Sample 2	1.483	0.018	0.023	1.077	0.022	0.440
Sample 3	1.341	-0.005	0.158	1.083	0.036	0.576
Sample 4	1.698	0.018	0.016	0.911	-0.001	0.391
Sample 5	1.493	-0.006	-0.010	1.097	-0.011	0.410
Sample 6	1.479	-0.010	0.051	1.067	-0.021	0.454

Table 1: ACG parameter estimates for the fiber orientation of the scaffolds.

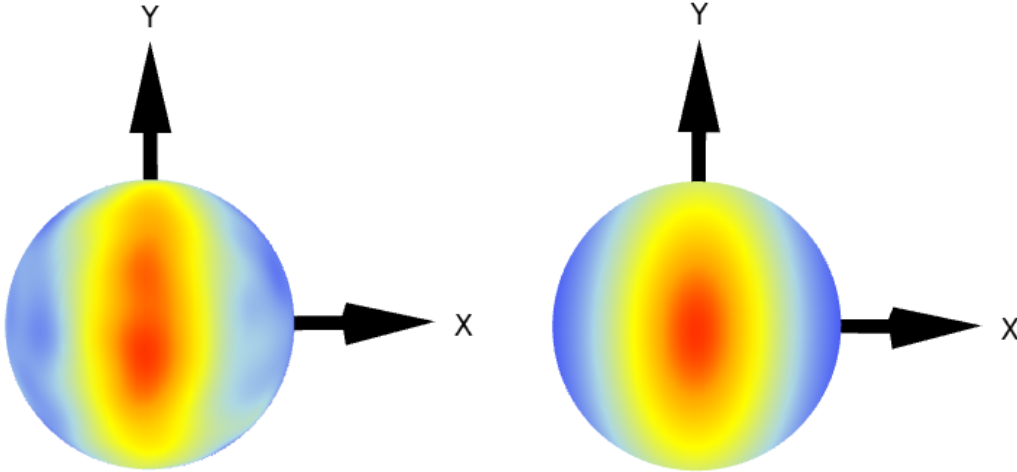


Figure 4: Spherical density plots of the empirical fiber orientation distribution (left) and of the fitted ACG model (right) for sample 1.

in \mathbb{R}^3 is given by

$$f_A(\theta) = \frac{1}{4\pi|\det A|^{\frac{1}{2}}}(\theta^T A^{-1}\theta)^{-\frac{3}{2}}, \quad \theta \in \mathbb{S}^2. \quad (3.1)$$

The ACG distribution can be interpreted as the distribution of the direction of a $\mathcal{N}_3(0, A)$ -distributed random vector or, alternatively, as the distribution of a random point uniformly distributed on the ellipsoid $\theta : \theta^T A^{-1}\theta = 1$. A sample for estimating the parameter matrix A is obtained by the fiber directions of a subsample of foreground (fiber) voxels in the image. Subsampling reduces the amount of data to an acceptable level. Moreover, neighboring voxels are highly dependent as they often belong to the same fiber. By subsampling, we were able to create a nearly independent data set, which is a prerequisite for the parameter estimation. Voxels were sampled by applying independent Bernoulli trials with $p = 1/100\,000$ to all voxels. Prior to the estimation, we rotated the orientations in each sample such that its principal direction was aligned with the x-axis. This way, we ensured comparability between samples.

We calculated the maximum likelihood estimate for the ACG parameter matrix A using the fixed-point algorithm proposed by Tyler [72]. For the results, see Table 1 and Fig. 4 for a visualization. To validate the goodness of fit, we inspected QQ plots for the longitude and colatitude [28]. The model quantiles were obtained by the empirical quantiles of a simulated sample of the fitted ACG model [58]. For all samples, the QQ plots indicate a good fit, see Fig. 10a - 12.

To determine the cell diffusion tensors (2.23), (2.24) we need to assess the mesoscopic orientation distribution of fibers $q(x, \theta)$ from the scaffold data. The analysis of the CT images does not give evidence of a strong local variation of the fiber direction distribution. Therefore, we will use $q(x, \theta) = q(\theta) = f_A(\theta)$ as determined in (3.1). The second moments can be determined according to the method in [53]: with $q(x, \theta) = f_A(\theta)$ we compute

$$\mathbb{D}_\beta = \int_{\mathbb{S}^2} \theta \otimes \theta q(x, \theta) d\theta = c_{A,\beta} \int_0^\infty \prod_{i=1}^3 (b_i + \zeta)^{-\frac{\beta_i+1}{2}} d\zeta, \quad (3.2)$$

where $\beta = (\beta_1, \beta_2, \beta_3)^T$ is a multiindex with $\sum_{i=1}^3 \beta_i = 2$ used to specify the entries in \mathbb{D}_β , b_i ($i = 1, 2, 3$) are the entries in $A^{-1} = \text{diag}(b_1, b_2, b_3)$, and

$$c_{A,\beta} := \frac{|\det A|^{-1/2}}{4} \prod_{i=1}^3 \frac{\beta_i!}{(\beta_i/2)!}.$$

The entries of \mathbb{D}_β can thus be obtained by computing the elliptic integrals in (3.2) above. For instance, $\mathbb{D}_{(2,0,0)} = \mathbb{D}_{11} = \frac{|\det A|^{-1/2}}{2} \int_0^\infty (b_1 + \zeta)^{-3/2} (b_2 + \zeta)^{-1/2} (b_3 + \zeta)^{-1/2} d\zeta$.

3.3 Biomechanical characterization of PET scaffolds

Materials and Methods

Scanning electron microscopy analysis of three-dimensional PET scaffolds Three-dimensional (3D) PET scaffolds were cut (diameter: 4mm , thickness: 1.85mm), process for critical point-drying. Afterwards, the samples fixed with carbon tape, and coated with a 20nm gold-palladium film to become electrically conductive. High-resolution images were acquired from PET surfaces in an environmental scanning electron microscope (SEM, S-5200, Hitachi, Tokyo, Japan) with an acceleration voltage of 15kV for qualitative assessment of the distribution of the fibres.

Indentation mapping A biomechanical indentation mapping of the PET scaffolds was performed to investigate the homogeneity of the scaffold's material properties. PET scaffolds with two different grammage ranges: $267 - 292\text{g/m}^2$ (LW) and $400 - 420\text{g/m}^2$ (HW) were tested. PET scaffolds sterilized by a dose of 25 kGy of gamma irradiation, as recommended for terminal sterilization of medical products, were also tested. All samples were analysed twice; before and after a 60 min hydration period with 10 ml phosphate buffer saline (PBS). Briefly, a multiaxial mechanical tester (MACH-1 v500css, Biomomentum Inc., Laval, QC, Canada) equipped with a 17N load cell was used to perform spatial stress relaxation tests on the surface of the PET scaffolds in accordance to an established algorithm [69]. First, the build-in camera-registration system was used to define a pattern with measurement points on the surface ($n=6$ measurement points). On each measurement point a non-destructive indentation relaxation test was performed using a spherical indenter ($\varnothing = 2\text{mm}$, indentation depth: $15\%h_0$ (initial sample height), velocity: $\sim 5\%h_0/\text{s}$, relaxation time: 10s). At each measurement point, the structural stiffness of the PET scaffolds was calculated [34].

Multi-step confined compression relaxation test Following the spatial indentation mapping [67], the viscoelastic properties of the PET scaffolds were further investigated under confined conditions in a material testing machine (Z10, ZwickRoell, Germany). 4,5 Cylindrical samples ($\varnothing = 4.6\text{mm}$) were punched out at the before tested measurement points using a biopsy punch (Stiefel Laboratories Inc, UK). For the stress-relaxation test, the sample was placed in a custom-made confined compression testing chamber filled with PBS 5. One side of the PET scaffolds was facing the impermeable bottom of a measuring chamber, and the opposite side was facing a porous ceramic (Al_2O_3) cylinder to allow free fluid flow. The measuring chamber had the same diameter ($\varnothing = 4.6\text{mm}$) as the samples, thus, confining their radial deformation. The materials testing machine equipped with a stainless-steel punch induced an initial preload of 0.1N to ensure the same testing conditions at the beginning of each test, while the thickness of the samples (h_0) was automatically registered. Then, the samples were loaded to three consecutive, incremental strain levels (ε_i) of 0.1 , 0.15 , and 0.2 at an individual sample loading rate of $100\%h_0/\text{min}$. Each strain level was held constant for 15 minutes to ensure an equilibrium state was reached. Sample strain was continuously measured and controlled using a laser displacement transducer (optoNC DT 2200-20, Micro-Epsilon GmbH & Co. KG, Germany, $0.3\mu\text{m}$ resolution, $\pm 0.03\%$ accuracy). The resulting force was measured by a 20N load cell (ZwickRoell, Germany) [66, 68].

Data analysis was performed using a custom-made MATLAB R2020a (MathWorks Inc, USA) script. At each strain rate, the equilibrium's modulus E_{eq} representing the matrix stiffness was calculated by the quotient of the stress at equilibrium ($\sigma_{t \rightarrow \infty}$) and the applied strain (ε_i):

$$E_{eq} = \frac{\sigma_{t \rightarrow \infty}}{\varepsilon_i}, \quad \varepsilon_i = 0.1, 0.15, 0.2. \quad (3.3)$$

Solving the diffusion equation of Mow et al. by means of nonlinear least squares regression strain rates yields the hydraulic permeability k as a measure of the resistance to fluid flow through the PET scaffolds

for all three strain levels. The aggregate modulus H indicates a combined modulus of both the fluid and the solid phase of the PET scaffolds [51]:

$$\sigma_t = \sigma_{t \rightarrow \infty} + 2H\varepsilon_i e^{-\left(\frac{\pi}{h_0}\right)^2 Hkt} \quad (3.4)$$

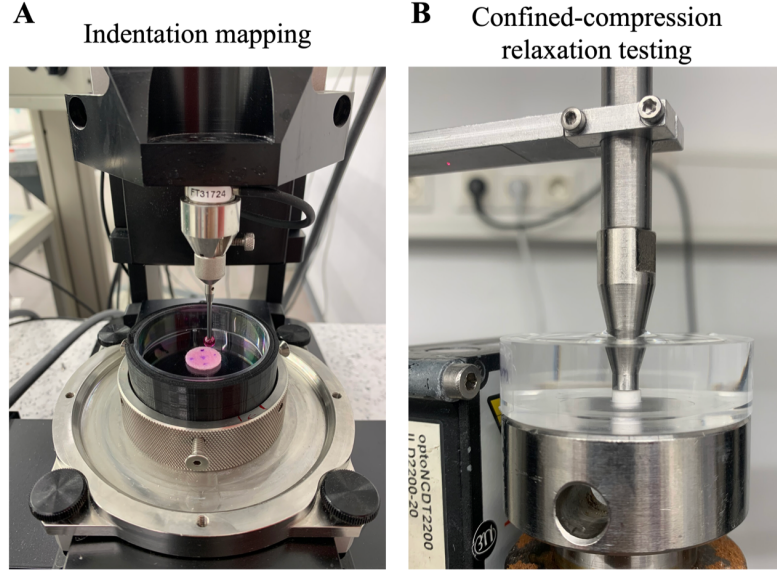


Figure 5: The PET scaffolds were mechanically investigated using two different testing methods: A) spatial indentation mapping was performed on the surface of the entire PET scaffold. Subsequently, cylindrical samples were punched out of the scaffolds to further analyse the biomechanical properties under B) confined-compression conditions.

Statistical analysis GraphPad Prism 9 software (GraphPad Software, Inc, La Jolla, CA, USA) was used for the statistical analysis. Normal distribution was assessed with the Shapiro-Wilk test. The data of the normal indentation tests were normally distributed. For the comparison between dry and hydrated conditions paired t-test was performed, while for the comparison between the non-sterile and sterile PET scaffolds and the comparison of the LW and HW PET samples unpaired t-test with Welch's correction was used. The results of the confined tests were analysed using Mann-Whitney testing. The level of significance was defined as $p < 0.05$.

Results

PET biomechanical characterization The scaffold punches collected from the PET (Figure 6 A, B) were prone to losing fibres with handling and displayed unorganized fibre distribution under SEM imaging (Figure 6 C, D).

No differences in the structural stiffness between the dry and hydrated state were observed for the PET scaffolds (Figure 7). When comparing the non-sterile and sterile LW samples, significantly higher K values were found for the sterile PET scaffolds both under dry and hydrated condition ($p < 0.0001$), whereas no differences were found between non-sterile and sterile HW scaffolds. The pairwise comparisons of the LW and HW scaffolds revealed significantly higher K values for the HW PET scaffolds both in the non-sterile and sterile groups (dry: $p < 0.01$; hydrated: $p < 0.001$).

No differences in the equilibrium modulus (E_{eq}) were found between the non-sterile and sterile samples in both the LW and HW PET scaffolds (Figure 8 A). At all strain levels, the non-sterile and sterile LW PET scaffolds indicated significantly lower E_{eq} values compared to the respect HW scaffolds ($p < 0.05$). For the permeability (k), no differences were found between the non-sterile and sterile samples at none of the three strain levels (Figure 8 B). The comparison between the LW and HW PET revealed no significant differences in all conditions. The aggregate modulus H_A was not significantly different when comparing the non-sterile and sterile samples in none of the three strain levels, neither for the LW nor the HW scaffolds (Figure 8 C). No differences in H_A were found when comparing the LW with the HW PET scaffolds in all three strain levels and in sterile versus non-sterile conditions.

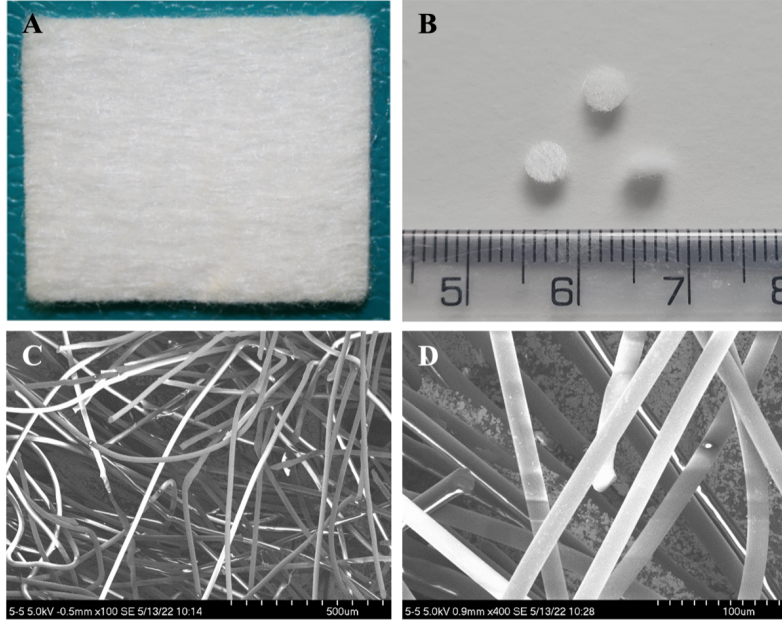


Figure 6: 3D PET scaffolds. A) Top view of PET sheet and B) top and peripheral view of PET punches. C, D) Representative scanning electron microscopy images from interior cross-section of PET samples at two different magnifications (scale bars indicate $500\mu m$ and $100\mu m$)

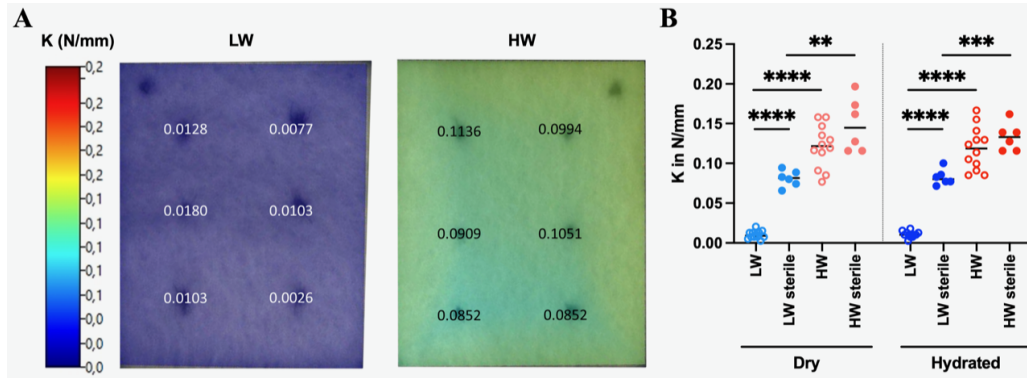


Figure 7: Results of the indentation mapping. A) Representative stiffness mappings of a LW non-sterile and HW non-sterile PET scaffold. B) Structural stiffness (K in N/mm) are shown for the low weight (LW) and high weight (HW) PET scaffolds in dry and hydrated condition, each for the non-sterile and sterile samples. $n = 6$ (sterile), $n = 12$ (non-sterile). $** p < 0.01$, $*** p < 0.001$, $**** p < 0.0001$.

4 Numerical methods

In this section, we summarize the numerical treatment of both the fluid flow simulation in the perfusion chamber and the cell dynamics in the scaffold. We start with the flow system (2.25)-(2.32), supplemented with mechanical effects as described in Section 2.2, and use FreeFem++ (version 4.1) for the spatial discretization. The codes are available on GitHub.

Let us define the spaces

$$\left\{ \begin{array}{l} V_f = \{\mathbf{v}_f \in H^1(\Omega_f)^d : \mathbf{v}_f = 0 \text{ on } \Gamma_f\}, \\ P_f = L^2(\Omega), \\ V_p = H(\text{div}; \Omega_p), \\ P_p = L^2(\Omega_p), \\ \Xi_p = \{\boldsymbol{\xi}_p \in H^1(\Omega_p)^d : \boldsymbol{\xi}_p = 0 \text{ on } \Gamma_p\}. \end{array} \right. \quad (4.1)$$

Using the variational formulation of (2.33a)-(2.33b)-(2.35)-(2.36), the following boundary terms at the interface Γ_I between scaffold and surrounding fluid flow appear:

$$-(\boldsymbol{\sigma}_p \mathbf{n}_p, \boldsymbol{\xi})_{\Gamma_I} + (p_p \mathbf{n}_p, \mathbf{v}_p)_{\Gamma_I} - (\boldsymbol{\sigma}_f \mathbf{n}_f, \mathbf{v}_f)_{\Gamma_I}, \quad (4.2)$$

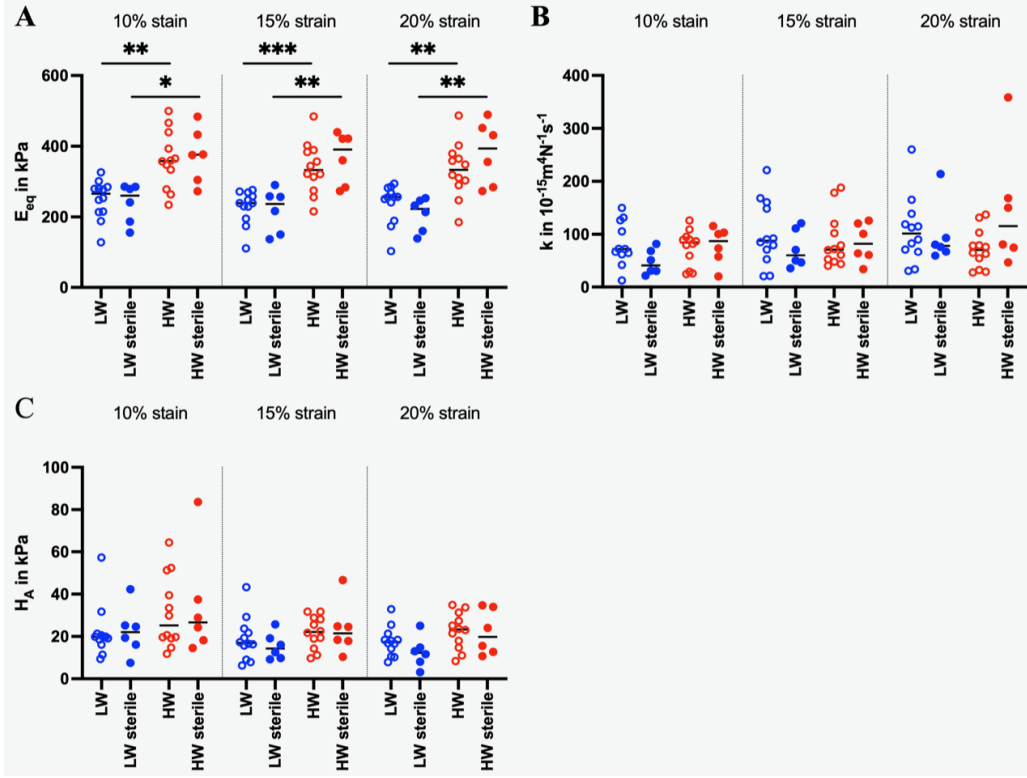


Figure 8: Results of the confined compression tests at 10%, 15% and 20% strain for the low weight (LW) and high weight (HW) PET scaffolds under non-sterile and sterile conditions. A) Equilibrium modulus (E_{eq} in kPa), B) permeability (k in $10^{-15}m^4N^{-1}s^{-1}$), and C) aggregate modulus (H_A in kPa). $n = 6$ (sterile), $n = 12$ (non-sterile). * $p < 0.05$, ** $p < 0.01$, *** $p < 0.001$.

with $\xi \in \Xi_p$, $\mathbf{v}_p \in V_p$ and $\mathbf{v}_f \in V_f$.

We set all variables to 0 for the initial conditions. We consider a referential fixed domain such that the surface Γ_I is perpendicular to the axis (Oz), $\mathbf{n}_f = (0, 0, -1)$ and the tangential vectors are given by $\mathbf{t}_1 = (1, 0, 0)$ and $\mathbf{t}_2 = (0, -1, 0)$. Then, we apply Nitsche's method as in [13], which allows us to correctly impose the mass conservation (2.37) with penalization terms. We obtain the following variational problem:

Find $(\mathbf{u}_f, p_f, \mathbf{u}_p, p_p, \eta_p) \in (V_f, P_f, V_p, P_p, \Xi_p)$ such that for all $(\mathbf{v}_f, q_f, \mathbf{v}_p, q_p, \xi_p) \in (V_f, P_f, V_p, P_p, \Xi_p)$

$$\left\{ \begin{array}{l} (\rho_f \partial_t \mathbf{u}_f, \mathbf{v}_f)_{\Omega_f} + 2\mu_f (D(\mathbf{u}_f), D(\mathbf{v}_f))_{\Omega_f} - (p_f, \nabla \cdot \mathbf{v}_f)_{\Omega_f} + (q_f, \nabla \cdot \mathbf{u}_f)_{\Omega_f} \\ + (\rho_p \partial_{tt} \eta_p, \xi_p)_{\Omega_p} + (\lambda_p \nabla \cdot \eta_p, \nabla \cdot \xi_p)_{\Omega_p} + (2\mu_p D(\eta_p), D(\xi_p))_{\Omega_p} - (\alpha p_p, \nabla \cdot \xi_p)_{\Omega_p} \\ + (\mu K^{-1} \mathbf{u}_p, \mathbf{v}_p)_{\Omega_p} - (p_p, \nabla \cdot \mathbf{v}_p)_{\Omega_p} \\ + \partial_t (\frac{1}{M} p_p, q_p)_{\Omega_p} + (\alpha \partial_t \nabla \cdot \eta_p, q_p)_{\Omega_p} + (\nabla \cdot \mathbf{u}_p, q_p)_{\Omega_p} \\ + I_\Gamma = -(p_{in}(t) \mathbf{n}_f, \mathbf{v}_f)_{\Gamma_{in}}, \end{array} \right. \quad (4.3)$$

where

$$I_\Gamma = \int_{\Gamma_I} \mathbf{n}_f \cdot \boldsymbol{\sigma}_f \mathbf{n}_f (\xi_p + \mathbf{v}_p - \mathbf{v}_f) \cdot \mathbf{n}_f + \int_{\Gamma_I} \gamma \mu_f h^{-1} (\mathbf{u}_f - \mathbf{u}_p - \partial_t \eta_p) \cdot \mathbf{n}_f (\mathbf{v}_f - \xi_p - \mathbf{v}_p) \cdot \mathbf{n}_f \\ - \int_{\Gamma_I} \alpha_{BJS} \mathbf{t} \cdot (\mathbf{u}_f - \partial_t \eta_p) (\xi_p - \mathbf{v}_f) \cdot \mathbf{t} + \int_{\Gamma_I} \mathbf{n}_f \cdot (q_f I + 2\mu D(\mathbf{v}_f)) \mathbf{n}_f (\partial_t \eta_p + \mathbf{u}_p - \mathbf{u}_f) \cdot \mathbf{n}_f, \quad (4.4)$$

and where h is the size of the mesh, and γ a penalization.

We proceed with direct simulations of the model for the cell dynamics (2.25)–(2.29) on the scaffold, denoted Ω_p . A numerical scheme should be locally mass conservative, thus we have decided to employ a first order Non-symmetric Interior Penalty discontinuous Galerkin (NIP dG) scheme in space [60]. We define a mesh \mathcal{T}_h of Ω_p and seek solutions c_1 , c_2 and χ in the broken polynomial space $\mathbb{P}_d^1(\mathcal{T}_h)$ given by $\mathbb{P}_d^1(\mathcal{T}_h) := \{u \in L^2(\Omega_p) \mid \forall T \in \mathcal{T}_h, v|_T \in \mathbb{P}_d^1(T)\}$, whereas we are looking for h and k on the classical $\mathbb{P}_d^1(\Omega_p)$ FE space. Multiplying by test functions ($\nu_{c_1}, \nu_{c_2}, \nu_{chi}, \nu_h, \nu_\tau$) and integrating over Ω_p , the system

(2.25)–(2.29) becomes

$$\left\{ \begin{array}{l} (\partial_t c_1, \nu_{c1}) + (\mathbb{D}_1 \nabla c_1, \nabla \nu_{c1}) + ([c_1], \{\mathbb{D}_1 \nabla \nu_{c1}\})_\Gamma - ([\nu_{c1}], \{\mathbb{D}_1 \nabla c_1\})_\Gamma \\ \quad - (\mathbf{v} \cdot c_1, \nabla \nu_{c1}) + ((\mathbf{v} c_1)^\uparrow, [\nu_{c1}])_{\partial \Omega_p} \\ \quad + (\alpha_1(\chi, S)c_1 - \frac{\omega_2}{\omega_1} \alpha_2(\chi, S)c_2 - \beta c_1(1 - c_1 - c_2), \nu_{c1}) + (\eta[c_1], [\nu_{c1}])_\Gamma = 0, \\ (\partial_t c_2, \nu_{c2}) + (\mathbb{D}_2 \nabla c_2, \nabla \nu_{c2}) + ([c_2], \{\mathbb{D}_2 \nabla \nu_{c2}\})_\Gamma \\ \quad - ([\nu_{c2}], \{\mathbb{D}_2 \nabla c_2\})_\Gamma - (\frac{\omega_2}{\omega_1} \alpha_1(S)c_1 - \alpha_2(S)c_2, \nu_{c2}) + (\eta[c_2], [\nu_{c2}])_\Gamma = 0, \\ (\partial_t \chi, \nu_\chi) + (D_\chi \nabla \chi, \nabla \nu_\chi) + ([\chi], \{D_\chi \nabla \nu_\chi\})_\Gamma - ([\nu_\chi], \{D_\chi \nabla \chi\})_\Gamma \\ \quad + (a_\chi(c_1 + c_2)) + (\eta[\chi], [\nu_\chi])_\Gamma = 0, \\ (\partial_t h, \nu_h) + (\gamma_1 h c_1, \nu_h) + (\gamma_2 h c_2, \nu_h) - (\frac{c_2}{1+c_2}, \nu_h) = 0, \\ (\partial_t \tau, \nu_\tau) + (\delta_1 \tau c_1, \nu_\tau) - (c_2, \nu_\tau) = 0, \\ c_1(0) = c_1^0, c_2(0) = c_2^0, h(0) = h_0, \tau(0) = \tau_0. \end{array} \right. \quad (4.5)$$

Here, ∇ refers to the broken gradient, Γ represents all the interfaces of the mesh, η is the penalization parameter, $\mathbf{v} = b_1 \nabla h + b_2 \nabla k$, (\cdot, \cdot) refers to the $L^2(\Omega_p)$ inner product, $(\cdot)^\uparrow$ is the upwind flux, and $[\cdot]$ and $\{\cdot\}$ refer to jumps and means. The nonlinear system (4.5) has then been discretized in time by implicit Euler, which needs Newton's method in each timestep.

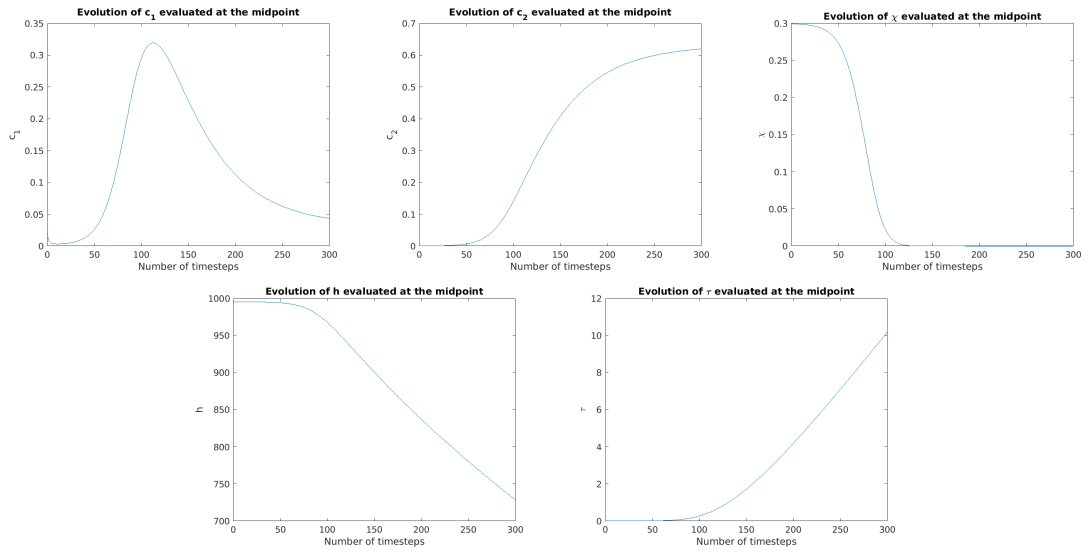
Figure 9 displays the results of a 2D simulation run for the cell dynamics with a time step $\Delta t = 0.1$ and the parameters presented in Table 2 in dimensionless form. The stress in the scaffold has been determined from the flow simulation as described in [32] and is kept constant here. As can be seen from the temporal behavior of the different densities evaluated in the midpoint of the scaffold, the hMSCs grow faster than the chondrocytes and reach a peak, after which the differentiation medium χ is completely consumed. While the concentration of hyaluron decays somewhat over time, the production of ECM continues over time. Additionally, the two snapshots of c_1 and c_2 illustrate the influence of the orientation distribution that is part of the computation of the diffusion tensor in (2.23). The cell dynamics is accelerated (due to the taxis term which models migration bias towards gradients of hyaluron - thus of scaffold fibre density and of ECM) along a diagonal line that represents the dominating orientation in the fibres of the scaffold. Since ECM is produced only by chondrocytes and these, in turn, are only obtained by differentiation of hMSCs, the taxis towards $\nabla \tau$ only accentuates the directional bias induced by the structure of the scaffold.

a_1	0.015	β	0.5
b_1	0.005	b_2	0.001
α_{min}	0.05	α_{max}	0.1
δ_1	0.1	γ_1	0.001
γ_2	0.005	$S_{min}-S_{max}$	0.1-0.3
s_1	30	s_2	15

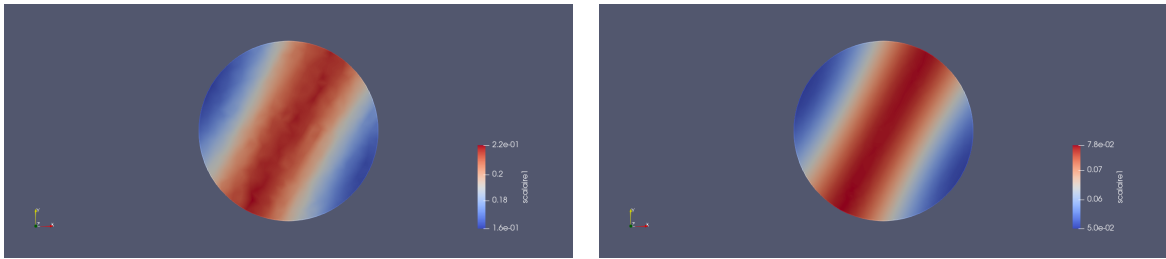
Table 2: Values of model parameters

5 Conclusions and perspectives

In this note we proposed a multiscale approach to deriving a mathematical model for spread and (de)differentiation of cells involved in tissue regeneration. Their dynamics are (one-way) coupled to fluid flow and scaffold deformation within a bioreactor. Moreover, we also accounted for the evolution of a differentiation medium and of hyaluron, which impregnates the scaffold and is assumed not to diffuse. The effective RDTEs obtained by parabolic upscaling from lower scales are macroscopic, but they carry in their motility terms information about microscopic and mesoscopic dynamics. They appear as a natural consequence of the upscaling process and are not imposed. Moreover, the hMSC diffusion tensor directly encodes the tissue topology. Our macroscopic model obtained here is somehow related to the one in [63], however extending it in the sense that we perform a more careful characterization of cell dynamics: on the one hand, we consider two cell phenotypes and their transitions; on the other hand, we pay enhanced attention to the anisotropic structure of the fibrous tissue in their surroundings. Instead of the nutrient dynamics considered in [63] we involved the evolution of a growth factor controlling (de)differentiation of cells and of a non-diffusing chemical cue (hyaluron) impregnating the scaffold. The simulations show that the cell patterns and thus the newly formed tissue are much influenced by the directional distribution of the scaffold's fibers, via taxis. The latter, in turn, was obtained during the upscaling process. In fact, the analysis performed in [49] for a simplified version of our macroscopic model shows that cell and tissue



(a) Evolution of c_1 , c_2 , χ , h and τ in the midpoint of the scaffold



(b) Snapshots of c_1 and c_2 at timestep 87. The preferred direction of cell spread is due to the fibre orientation distribution and the corresponding haptotaxis of hMSCs towards gradients of h and τ .

Figure 9: Cell dynamics in the scaffold, 2D simulation

patterns are triggered by taxis and not by diffusion.

To our knowledge this is the first model for tissue regeneration which includes in an explicit manner the anisotropic topology of the scaffold, statistically assessed from CT data. Furthermore, this is the first approach to simultaneously account for the dynamics of MSCs and their differentiated, matrix-producing counterparts, along with biochemical factors and mechanical effects triggered by fluid flow in a bioreactor and therewith induced deformations of scaffold and ECM. The equations are informed by experimental data. This development was only possible in an interdisciplinary team contributing knowledge from several areas: scaffold production and cell seeding experiments (biomedical engineering), statistics (data processing), and in silico modeling (mathematics).

Our approach combining in vitro experiments with in silico modeling opens the way for investigating a broad palette of questions related to (meniscus) tissue regeneration. Among these, of particular interest are the roles played by geometry, anisotropy, and mechanical properties of the scaffold, along with phenotype preservation/switch of MSCs seeded in the scaffold under biochemical and biophysical influences.

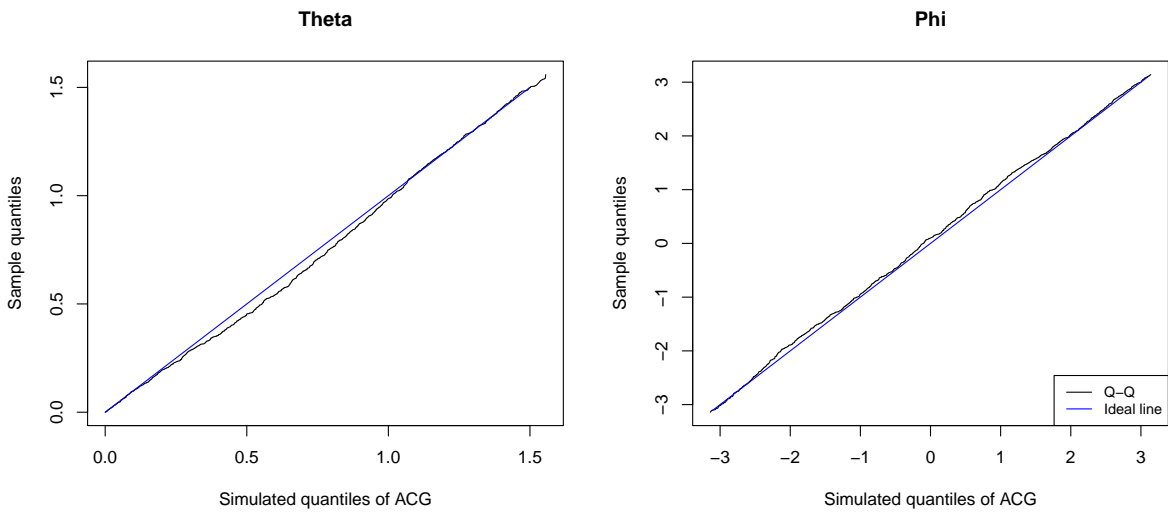
The developed models do not only inform the biomedical experiments by suggesting new conjectures and hypotheses, but they also arise interesting mathematical challenges in connection to the analysis (in terms of rigorous convergence of upscaling, well-posedness, patterning, and long term behavior) and numerics of such complex, nonlinear systems coupling equations of several different types and describing processes taking place on different time and space scales.

Acknowledgements

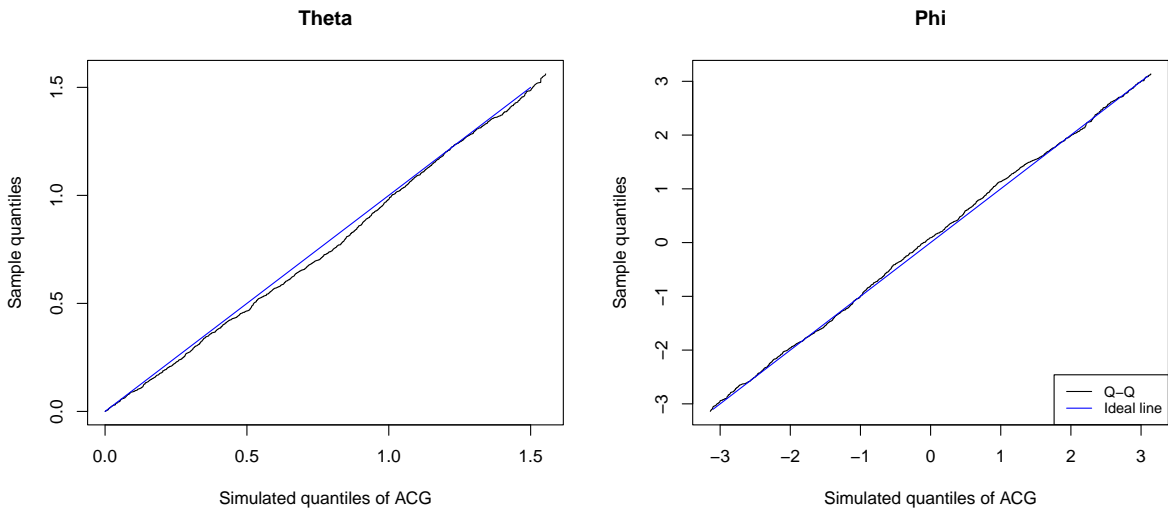
This work was funded by the German Research Foundation DFG within SPP 2311. We also acknowledge the support of MathApp at the RPTU Kaiserslautern-Landau. The authors would like to thank Pierre Jolivet (University of Sorbonne, CNRS) for helping with the parallelization of the code, as well as Nishith Mohan and Konstantin Hauch (RPTU Kaiserslautern-Landau) for pointing to us the moment assessment from [53] and for image preprocessing, respectively.

Appendix

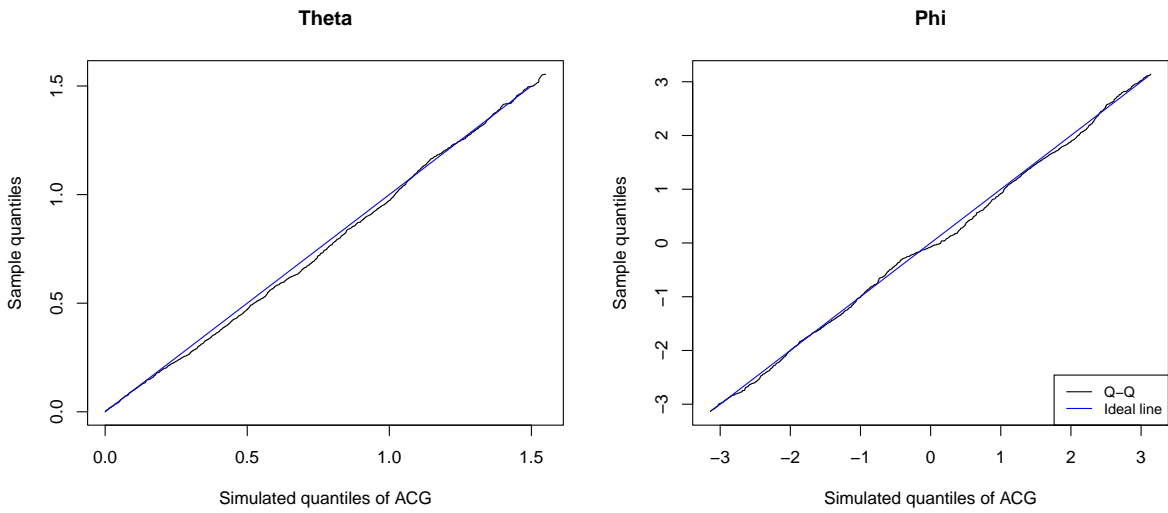
A QQ plots for ACG parameter estimation



(a) Sample 0.

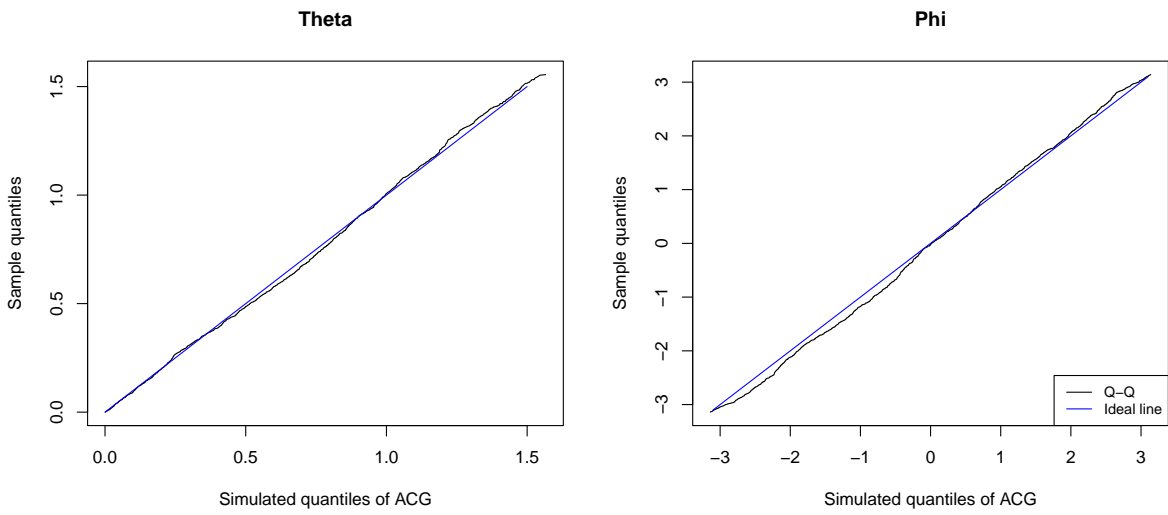


(b) Sample 1.

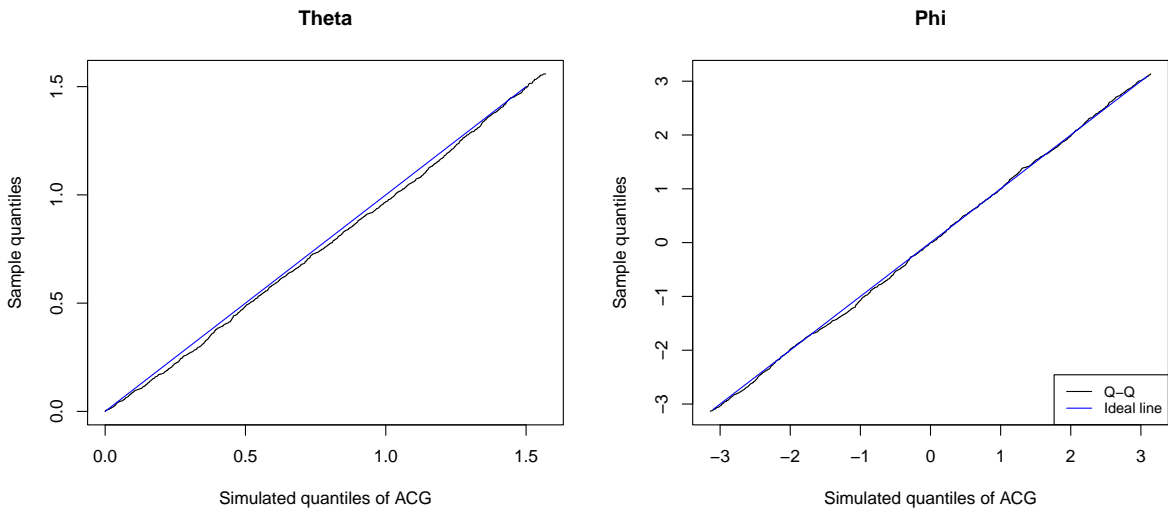


(c) Sample 2.

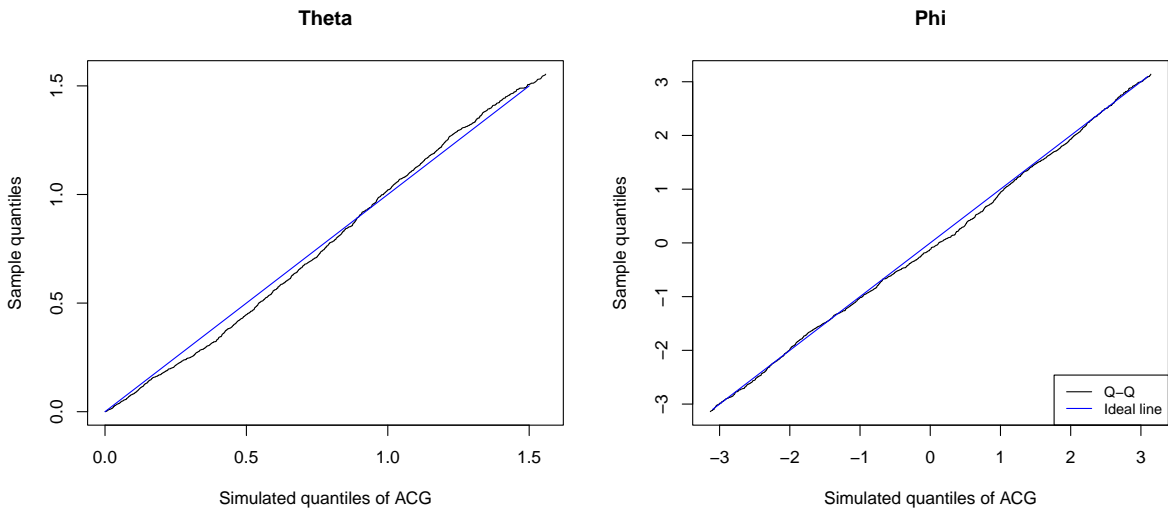
Figure 10: QQ plot for the ACG parameter estimation.



(a) Sample 3.



(b) Sample 4.



(c) Sample 5.

Figure 11: QQ plot for the ACG parameter estimation.

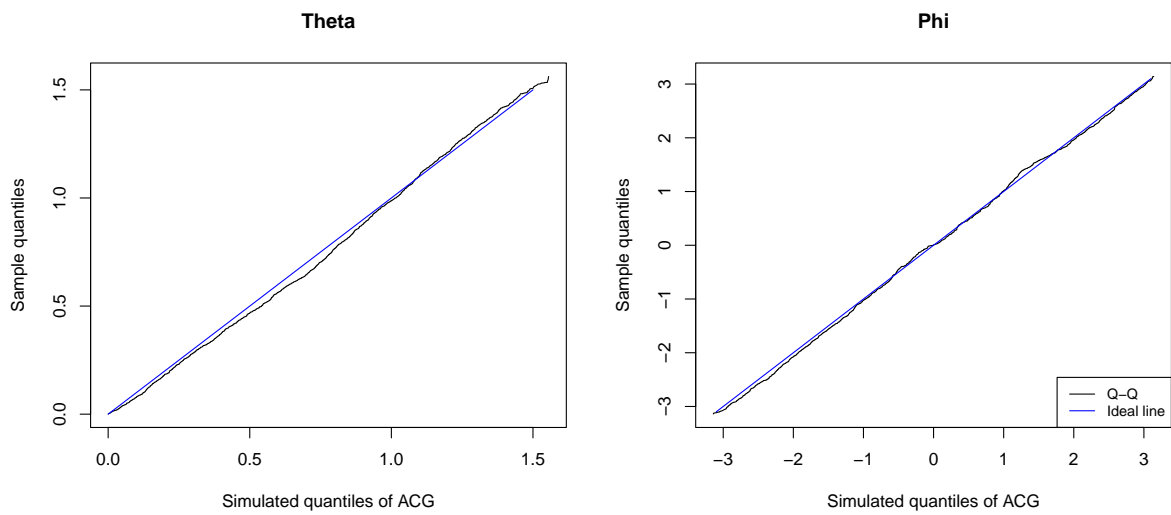


Figure 12: QQ plot for the ACG parameter estimation of sample 6.

References

- [1] G. H. Altman, R. L. Horan, I. Martin, J. Farhadi, P. R. Stark, V. Volloch, J. C. Richmond, G. Vunjak-Novakovic, and D. L. Kaplan. “Cell differentiation by mechanical stress”. In: *The FASEB Journal* 16.2 (2002), pp. 1–13.
- [2] I. Ambartsumyan, E. Khattatov, I. Yotov, and P. Zunino. “A Lagrange multiplier method for a Stokes–Biot fluid–poroelastic structure interaction model”. In: *Numerische Mathematik* 140.2 (2018), pp. 513–553.
- [3] A. Andreykiv, F. Van Keulen, and P. Prendergast. “Simulation of fracture healing incorporating mechanoregulation of tissue differentiation and dispersal/proliferation of cells”. In: *Biomechanics and modeling in mechanobiology* 7 (2008), pp. 443–461.
- [4] S. Astanin and L. Preziosi. “Multiphase Models of Tumour Growth”. In: *Selected Topics in Cancer Modeling: Genesis - Evolution - Immune Competition - Therapy*. Ed. by N. Bellomo, M. Chaplain, and E. D. Angelis. Springer, 2008, pp. 1–31.
- [5] A. C. AufderHeide and K. A. Athanasiou. “Mechanical stimulation toward tissue engineering of the knee meniscus”. In: *Annals of biomedical engineering* 32 (2004), pp. 1163–1176.
- [6] A. Bailón-Plaza and M. C. Van der Meulen. “A Mathematical Framework to Study the Effects of Growth Factor Influences on Fracture Healing”. In: *Journal of Theoretical Biology* 212.2 (2001), pp. 191–209.
- [7] V. H. Barocas and R. T. Tranquillo. “An Anisotropic Biphasic Theory of Tissue-Equivalent Mechanics: The Interplay Among Cell Traction, Fibrillar Network Deformation, Fibril Alignment, and Cell Contact Guidance”. In: *Journal of Biomechanical Engineering* 119.2 (1997), pp. 137–145.
- [8] V. H. Barocas and R. T. Tranquillo. “Biphasic Theory and In Vitro Assays of Cell-Fibril Mechanical Interactions in Tissue-Equivalent Gels”. In: *Cell Mechanics and Cellular Engineering*. Springer New York, 1994, pp. 185–209.
- [9] V. H. Barocas and R. T. Tranquillo. “An anisotropic biphasic theory of tissue-equivalent mechanics: the interplay among cell traction, fibrillar network deformation, fibril alignment, and cell contact guidance”. In: (1997).
- [10] N. Bellomo, A. Bellouquid, L. Gibelli, and N. Outada. *A quest towards a mathematical theory of living systems*. Springer, 2017.
- [11] N. Bellomo, A. Bellouquid, Y. Tao, and M. Winkler. “Toward a mathematical theory of Keller–Segel models of pattern formation in biological tissues”. In: *Mathematical Models and Methods in Applied Sciences* 25.09 (2015), pp. 1663–1763.
- [12] E. Borgiani, G. N. Duda, and S. Checa. “Multiscale Modeling of Bone Healing: Toward a Systems Biology Approach”. In: *Frontiers in Physiology* 8 (2017).
- [13] M. Bukač, I. Yotov, R. Zakerzadeh, and P. Zunino. “Partitioning strategies for the interaction of a fluid with a poroelastic material based on a Nitsche’s coupling approach”. In: *Computer Methods in Applied Mechanics and Engineering* 292 (2015), pp. 138–170.
- [14] K. Campbell, S. Naire, and J. H. Kuiper. “A mathematical model of cartilage regeneration after chondrocyte and stem cell implantation – I: the effects of growth factors”. In: *Journal of Tissue Engineering* 10 (2019), p. 204173141982779.
- [15] K. Campbell, S. Naire, and J. H. Kuiper. “A mathematical model of cartilage regeneration after chondrocyte and stem cell implantation – II: the effects of co-implantation”. In: *Journal of Tissue Engineering* 10 (2019), p. 204173141982779.
- [16] L. Chen, K. Painter, C. Surulescu, and A. Zhigun. “Mathematical models for cell migration: a non-local perspective”. In: *Philosophical Transactions of the Royal Society B: Biological Sciences* 375.1807 (2020), p. 20190379.
- [17] S. Chiu, D. Stoyan, W. Kendall, and J. Mecke. *Stochastic geometry and its applications*. John Wiley & sons, 2013.
- [18] M. Conte, Y. Dzierma, S. Knobe, and C. Surulescu. “Mathematical modeling of glioma invasion and therapy approaches via kinetic theory of active particles”. In: *Mathematical Models and Methods in Applied Sciences* (2023), pp. 1–43.
- [19] M. Conte and C. Surulescu. “Mathematical modeling of glioma invasion: acid-and vasculature mediated go-or-grow dichotomy and the influence of tissue anisotropy”. In: *Applied Mathematics and Computation* 407 (2021), p. 126305.

- [20] G. Corbin, A. Klar, C. Surulescu, C. Engwer, M. Wenske, J. Nieto, and J. Soler. “Modeling glioma invasion with anisotropy-and hypoxia-triggered motility enhancement: From subcellular dynamics to macroscopic PDEs with multiple taxis”. In: *Mathematical Models and Methods in Applied Sciences* 31.01 (2021), pp. 177–222.
- [21] A. Dietrich, N. Kolbe, N. Sfakianakis, and C. Surulescu. “Multiscale modeling of glioma invasion: from receptor binding to flux-limited macroscopic PDEs”. In: *Multiscale Modeling & Simulation* 20.2 (2022), pp. 685–713.
- [22] D. Eberly, R. Gardner, B. Morse, S. Pizer, and C. Scharlach. “Ridges for image analysis”. In: *J. Mathematical Imaging and Vision* 4.4 (1994), 353–373. <https://doi.org/10.1007/BF01262402>.
- [23] M. Eckardt, K. J. Painter, C. Surulescu, and A. Zhigun. “Nonlocal and local models for taxis in cell migration: a rigorous limit procedure”. In: *Journal of Mathematical Biology* 81 (2020), pp. 1251–1298.
- [24] C. Engwer, T. Hillen, M. Knappitsch, and C. Surulescu. “Glioma follow white matter tracts: a multiscale DTI-based model”. In: *Journal of mathematical biology* 71 (2015), pp. 551–582.
- [25] C. Engwer, A. Hunt, and C. Surulescu. “Effective equations for anisotropic glioma spread with proliferation: a multiscale approach and comparisons with previous settings”. In: *Mathematical medicine and biology: a journal of the IMA* 33.4 (2016), pp. 435–459.
- [26] S. Evje and M. Winkler. “Mathematical Analysis of Two Competing Cancer Cell Migration Mechanisms Driven by Interstitial Fluid Flow”. In: *Journal of Nonlinear Science* 30.4 (2020), pp. 1809–1847.
- [27] N. Fahy, M. Alini, and M. J. Stoddart. “Mechanical stimulation of mesenchymal stem cells: Implications for cartilage tissue engineering”. In: *Journal of Orthopaedic Research* 36.1 (2018), pp. 52–63.
- [28] N. I. Fisher, T. Lewis, and B. J. J. Embleton. *Statistical Analysis of Spherical Data*. Cambridge [Cambridgeshire] ; New York: Cambridge University Press, 1987. 329 pp.
- [29] U Freymann, M Endres, U Goldmann, M Sittinger, and C Kaps. “Toward scaffold-based meniscus repair: effect of human serum, hyaluronic acid and TGF- β 3 on cell recruitment and re-differentiation”. In: *Osteoarthritis and Cartilage* 21.5 (2013), pp. 773–781.
- [30] L. Geris, A. Gerisch, J. Vander Sloten, R. Weiner, and H. Van Oosterwyck. “Angiogenesis in bone fracture healing: a bioregulatory model”. In: *Journal of theoretical biology* 251.1 (2008), pp. 137–158.
- [31] L. Ghasemi-Mobarakeh, M. P. Prabhakaran, L. Tian, E. Shamirzaei-Jeshvaghani, L. Dehghani, and S. Ramakrishna. “Structural properties of scaffolds: crucial parameters towards stem cells differentiation”. In: *World journal of stem cells* 7.4 (2015), p. 728.
- [32] E. Grosjean, B. Simeon, and C. Surulescu. “A mathematical model for meniscus cartilage regeneration”. In: *PAMM* 23.3 (2023).
- [33] M. Gómez-Benito, J. García-Aznar, J. Kuiper, and M. Doblaré. “Influence of fracture gap size on the pattern of long bone healing: a computational study”. In: *Journal of Theoretical Biology* 235.1 (2005), 105–119.
- [34] W. Hayes, L. Keer, G. Herrmann, and L. Mockros. “A mathematical analysis for indentation tests of articular cartilage”. In: *Journal of Biomechanics* 5.5 (Sept. 1972), pp. 541–551.
- [35] E. C. Holden, S. J. Chapman, B. S. Brook, and R. D. O’Dea. “A multiphase multiscale model for nutrient-limited tissue growth, part II: a simplified description”. In: *The ANZIAM Journal* 61.4 (2019), 368–381.
- [36] R. Huiskes, W. V. Driel, P. J. Prendergast, K. Søballe, et al. “A biomechanical regulatory model for periprosthetic fibrous-tissue differentiation”. In: *Journal of materials science: Materials in medicine* 8.12 (1997), pp. 785–788.
- [37] T. L. Jackson and H. M. Byrne. “A mechanical model of tumor encapsulation and transcapsular spread”. In: *Mathematical biosciences* 180.1-2 (2002), pp. 307–328.
- [38] P. A. Janmey and C. A. McCulloch. “Cell mechanics: integrating cell responses to mechanical stimuli”. In: *Annu. Rev. Biomed. Eng.* 9 (2007), pp. 1–34.
- [39] V. Klika, E. A. Gaffney, Y.-C. Chen, and C. P. Brown. “An overview of multiphase cartilage mechanical modelling and its role in understanding function and pathology”. In: *journal of the mechanical behavior of biomedical materials* 62 (2016), pp. 139–157.

- [40] N. Kolbe, N. Sfakianakis, C. Stinner, C. Surulescu, and J. Lenz. “Modeling multiple taxis: tumor invasion with phenotypic heterogeneity, haptotaxis, and unilateral interspecies repellence”. In: *Discr. Cont. Dyn. Syst. B* 26 (2021), pp. 443–481.
- [41] P. Kumar, J. Li, and C. Surulescu. “Multiscale modeling of glioma pseudopalisades: contributions from the tumor microenvironment”. In: *Journal of Mathematical Biology* 82 (2021), pp. 1–45.
- [42] P. Kumar, C. Surulescu, and A. Zhigun. “Multiphase modelling of glioma pseudopalisading under acidosis”. In: *arXiv preprint arXiv:2106.15241* (2021).
- [43] C Lee, S Grad, M Wimmer, M Alini, et al. “The influence of mechanical stimuli on articular cartilage tissue engineering”. In: *Topics in tissue engineering* 2.2 (2006).
- [44] G Lemon and J. King. “Travelling-wave behaviour in a multiphase model of a population of cells in an artificial scaffold”. In: *Journal of Mathematical Biology* 55 (2007), pp. 449–480.
- [45] G. Lemon, J. R. King, H. M. Byrne, O. E. Jensen, and K. M. Shakesheff. “Mathematical modelling of engineered tissue growth using a multiphase porous flow mixture theory”. In: *Journal of Mathematical Biology* 52.5 (2006), 571–594.
- [46] T. Lorenz and C. Surulescu. “On a class of multiscale cancer cell migration models: Well-posedness in less regular function spaces”. In: *Mathematical Models and Methods in Applied Sciences* 24.12 (Aug. 2014), pp. 2383–2436.
- [47] R. L. Mauck, G. J. Martinez-Diaz, X. Yuan, and R. S. Tuan. “Regional multilineage differentiation potential of meniscal fibrochondrocytes: implications for meniscus repair”. In: *The Anatomical Record: Advances in Integrative Anatomy and Evolutionary Biology: Advances in Integrative Anatomy and Evolutionary Biology* 290.1 (2007), pp. 48–58.
- [48] Y. Mishima and M. Lotz. “Chemotaxis of human articular chondrocytes and mesenchymal stem cells”. In: *Journal of Orthopaedic Research* 26.10 (2008), pp. 1407–1412.
- [49] S. C. Mohanan, N. Mohan, and C. Surulescu. “On a mathematical model for tissue regeneration”. In: *arXiv:2403.04516* (2024).
- [50] S. J. Mousavi and M. Hamdy Doweidar. “Role of mechanical cues in cell differentiation and proliferation: a 3D numerical model”. In: *PloS one* 10.5 (2015), e0124529.
- [51] V. C. Mow and R. Huiskes. “Structure and function of articular cartilage and meniscus”. In: *Basic Orthopaedic Biomechanics & Mechano-Biology*. Ed. by V. C. Mow, W. Gu, and F. H. Chen. Philadelphia: Lippincott Williams & Wilkins, 2005, pp. 182–257.
- [52] J. Ohser and K. Schladitz. *3d Images of Materials Structures – Processing and Analysis*. Weinheim: Wiley VCH, 2009.
- [53] F. Ospald. “Contributions to the Simulation and Optimization of the Manufacturing Process and the Mechanical Properties of Short Fiber-Reinforced Plastic Parts”. PhD thesis. TU Chemnitz, 2019.
- [54] H. G. Othmer and T. Hillen. “The Diffusion Limit of Transport Equations Derived from Velocity-Jump Processes”. In: *SIAM J. Appl. Math.* 61 (2000), pp. 751–775.
- [55] N. Otsu. “A threshold selection method from gray level histograms”. In: *IEEE Trans. Systems, Man and Cybernetics* 9 (Mar. 1979), pp. 62–66.
- [56] R. D. O’Dea, M. R. Nelson, A. J. El Haj, S. L. Waters, and H. M. Byrne. “A multiscale analysis of nutrient transport and biological tissue growth in vitro”. In: *Mathematical Medicine and Biology* 32.3 (2014), 345–366.
- [57] K. Painter and T. Hillen. “Mathematical modelling of glioma growth: the use of diffusion tensor imaging (DTI) data to predict the anisotropic pathways of cancer invasion”. In: *Journal of theoretical biology* 323 (2013), pp. 25–39.
- [58] M. Papadakis, M. Tsagris, M. Dimitriadis, S. Fafalios, I. Tsamardinos, M. Fasiolo, G. Borboudakis, J. Burkardt, C. Zou, K. Lakiotaki, and C. Chatzipantsiou. *Rfast: A Collection of Efficient and Extremely Fast R Functions*. R package version 2.0.8. 2023.
- [59] J.-H. Park, T. Ushida, and T. Akimoto. “Control of cell differentiation by mechanical stress”. In: *The journal of physical fitness and sports medicine* 2.1 (2013), pp. 49–62.
- [60] D. A. D. Pietro and A. Ern. *Mathematical Aspects of Discontinuous Galerkin Methods*. Springer Berlin Heidelberg, 2012.

- [61] P. Pinter, S. Dietrich, B. Bertram, L. Kehrer, P. Elsner, and K. Weidenmann. “Comparison and error estimation of 3D fibre orientation analysis of computed tomography image data for fibre reinforced composites”. In: *NDT & E Int.* 95. <https://doi.org/10.1016/j.ndteint.2018.01.001> (2018).
- [62] R. G. Plaza. “Derivation of a bacterial nutrient-taxis system with doubly degenerate cross-diffusion as the parabolic limit of a velocity-jump process”. In: *Journal of Mathematical Biology* 78.6 (2019), pp. 1681–1711.
- [63] J. V. Pohlmeier and L. J. Cummings. “Cyclic Loading of Growing Tissue in a Bioreactor: Mathematical Model and Asymptotic Analysis”. In: *Bulletin of Mathematical Biology* 75.12 (2013), 2450–2473.
- [64] P. Prendergast, R. Huijskes, and K. Søballe. “Biophysical stimuli on cells during tissue differentiation at implant interfaces”. In: *Journal of Biomechanics* 30.6 (1997), pp. 539–548.
- [65] F. O. Ribeiro, M. J. Gómez-Benito, J. Folgado, P. R. Fernandes, and J. M. García-Aznar. “In silico Mechano-Chemical Model of Bone Healing for the Regeneration of Critical Defects: The Effect of BMP-2”. In: *PLOS ONE* 10.6 (2015). Ed. by M. Yamamoto, e0127722.
- [66] M. Saranya, A. M. da Silva, H. Karjalainen, G. Klinkenberg, R. Schmid, B. McDonagh, P. P. Molesworth, M. S. Sigfúsdóttir, A. M. Wågbo, S. G. Santos, C. Couto, V.-P. Karjalainen, S. D. Gupta, T. Järvinen, L. de Roy, A. M. Seitz, M. Finnilä, S. Saarakkala, A. M. Haaparanta, L. Janssen, and G. S. Lorite. “Magnetic-Responsive Carbon Nanotubes Composite Scaffolds for Chondrogenic Tissue Engineering”. In: *Advanced Healthcare Materials* (2023).
- [67] A. M. Seitz, F. Osthaus, J. Schwer, D. Warnecke, M. Faschingbauer, M. Sgroi, A. Ignatius, and L. Dürselen. “Osteoarthritis-Related Degeneration Alters the Biomechanical Properties of Human Menisci Before the Articular Cartilage”. In: *Frontiers in Bioengineering and Biotechnology* 9 (2021).
- [68] A. M. Seitz, F. Galbusera, C. Kraus, A. Ignatius, and L. Dürselen. “Stress-relaxation response of human menisci under confined compression conditions”. In: *Journal of the Mechanical Behavior of Biomedical Materials* 26 (2013), pp. 68–80.
- [69] S. Sim, A. Chevrier, M. Garon, E. Quenneville, P. Lavigne, A. Yaroshinsky, C. D. Hoemann, and M. D. Buschmann. “Electromechanical probe and automated indentation maps are sensitive techniques in assessing early degenerated human articular cartilage”. In: *Journal of Orthopaedic Research* 35.4 (2016), pp. 858–867.
- [70] C. Stinner, C. Surulescu, and A. Uatay. “Global existence for a go-or-grow multiscale model for tumor invasion with therapy”. In: *Mathematical Models and Methods in Applied Sciences* 26.11 (2016), pp. 2163–2201.
- [71] C. Stinner, C. Surulescu, and M. Winkler. “Global weak solutions in a PDE-ODE system modeling multiscale cancer cell invasion”. In: *SIAM Journal on Mathematical Analysis* 46.3 (2014), pp. 1969–2007.
- [72] D. E. Tyler. “Statistical analysis for the angular central Gaussian distribution on the sphere”. In: *Biometrika* 74.3 (1987), pp. 579–589.
- [73] S. L. Waters, L. J. Schumacher, and A. J. El Haj. “Regenerative medicine meets mathematical modelling: developing symbiotic relationships”. In: *npj Regenerative Medicine* 6.1 (2021).
- [74] O. Wirjadi, K. Schladitz, P. Easwaran, and J. Ohser. “Estimating Fibre Direction Distributions of Reinforced Composites from Tomographic Images”. In: *Image Anal. Stereol.* 35.3 (2016), 167–179 <http://dx.doi.org/10.5566/ias.1489>.
- [75] A. Zhigun and C. Surulescu. “A novel derivation of rigorous macroscopic limits from a micro-meso description of signal-triggered cell migration in fibrous environments”. In: *SIAM Journal on Applied Mathematics* 82.1 (2022), pp. 142–167.
- [76] A. Zhigun, C. Surulescu, and A. Hunt. “A strongly degenerate diffusion-haptotaxis model of tumour invasion under the go-or-grow dichotomy hypothesis”. In: *Mathematical Methods in the Applied Sciences* 41.6 (2018), pp. 2403–2428.
- [77] A. Zhigun, C. Surulescu, and A. Uatay. “Global existence for a degenerate haptotaxis model of cancer invasion”. In: *Zeitschrift für angewandte Mathematik und Physik* 67 (2016), pp. 1–29.